Title

Single-particle mapping of nonequilibrium nanocrystal transformations

Journal

Science, 354(6314)

ISSN

0036-8075

Authors

Ye, Xingchen

Jones, Matthew R

Frechette, Layne B

et al.

Publication Date

2016-11-18

DOI

10.1126/science.aah4434

Peer reviewed

Title: Direct Mapping of the Evolution of Individual Nanocrystals Undergoing Highly Non-Equilibrium Chemical Transformations

Authors:

Xingchen Ye,[#,†] Matthew R. Jones,[#,†] Layne B. Frechette,[†] Qian Chen,[†,▽] Alexander S. Powers,[†] Peter Ercius,[¶] Gabriel Dunn,[‡] Grant M Rotskoff,[£] Son C. Nguyen,[†] Vivekananda P Adiga,[‡] Alex Zettl,[‡,ǁ,§] Eran Rabani,[†,ǁ,ǂ] Phillip L. Geissler,[†] and A. Paul Alivisatos[*,†,¥,ǁ,§]

Affiliations:

[†]Department of Chemistry, [▽]Miller Institute for Basic Research in Science, [‡]Department of Physics, [¥]Department of Materials Science and Engineering, [£]Biophysics Graduate Group, University of California, Berkeley, Berkeley CA 94720, United States

[ǁ]Materials Sciences Division, [¶]The Molecular Foundry, Lawrence Berkeley National Laboratory, Berkeley, California 94720, United States

[§]Kavli Energy NanoScience Institute, University of California Berkeley and Lawrence Berkeley National Lab, Berkeley, CA 94720, United States

[ǂ]The Raymond and Beverly Sackler Center for Computational Molecular and Materials Science, Tel Aviv University, Tel Aviv 69978, Israel

[#]These authors contributed equally.

[*]To whom correspondence should be addressed.

E-mail: alivis@berkeley.edu

Abstract:

Chemists have developed mechanistic insight into numerous chemical reactions by thoroughly characterizing non-equilibrium species. While methods to probe these processes are

well-established for molecules, analogous techniques for, and understanding of intermediate structures in, nanomaterials have been lacking. We monitor the shape evolution of individual anisotropic gold nanostructures as they are oxidatively etched in a graphene liquid cell with a controlled redox environment. Short-lived, non-equilibrium nanocrystals are observed, structurally analyzed, and rationalized through Monte Carlo simulations. Understanding these reaction trajectories and their transient intermediates provides important mechanistic insight regarding nanocrystal reactivity and demonstrates the importance of developing tools capable of probing short-lived nanoscale species at the single particle level.

Main Text:

Nanoscience relies strongly on the ability to create highly non-equilibrium states of matter in which metastable materials are spatially organized in close proximity to yield desired properties. As a result, much effort is currently dedicated to understanding and controlling the complex pathways of formation,(*1*) transformation,(*2-5*) and dissolution(*6, 7*) of individual nanoscale building blocks. The majority of studies that have sought to understand the time course of nanocrystal-based chemical reactions have relied on methods to isolate intermediates and characterize them by electron microscopy or probe the ensemble via spectroscopic techniques. While these approaches have provided new fundamental knowledge, their time-resolution is severely limited and/or the ensemble averaging can obscure the details of individual pathways.

Methods for the direct imaging of the evolution of individual nanoparticle species in a liquid environment are under active development since they enable the preservation of dynamic processes present in the native colloid.(*1, 8-14*) Recently, our group has developed TEM liquid

cells based on the trapping of thin fluids between sheets of graphene (Fig. 1a).(*15*) The superior electron transparency of these windows has allowed for detailed tracking of nucleation and growth phenomena as well as atomistic reconstruction of nanocrystals.(*15, 16*)

To date, the majority of liquid-phase electron microscopy studies of transient nanoscale phenomena have focused on beam-induced nucleation and growth processes.(*1, 9, 10, 15, 17, 18*) These studies often produce an ill-defined set of randomly oriented nanoparticles that requires atomic resolution to deduce crystallographically-meaningful information about liquid phase phenomena.(*1, 15*) If, on the other hand, one monitors the *dissolution* of pre-synthesized particles with a well-defined crystallographic habit (vis-à-vis their shape), far more information is available regarding non-equilibrium processes since the orientation, zone axis, and exposed crystal facets can be known ahead of time and can be monitored kinetically via the evolution of particle shape over time.

In this work, we utilize graphene liquid cell TEM to monitor in real-time, at the single-particle level, non-equilibrium structural transformations of anisotropic gold nanocrystals as they undergo oxidative dissolution in their native aqueous environment (Fig. 1, Fig. S1-S3). Here, $FeCl_3$ is introduced as the primary oxidative etchant, the concentration of which allows for a controlled rate of etching in the presence of the electron beam, with virtually no etching in the absence of the beam (Fig. 1a). Oxidizing species such as OH radicals that are known radiolysis products induced by the electron beam act to trigger the reactions observed here (Fig. S4-S9, Movies S3-S8).(*17, 19*) Monte Carlo simulations corroborate the observation of non-equilibrium nanocrystal reaction pathways and shed light on their mechanistic underpinnings.

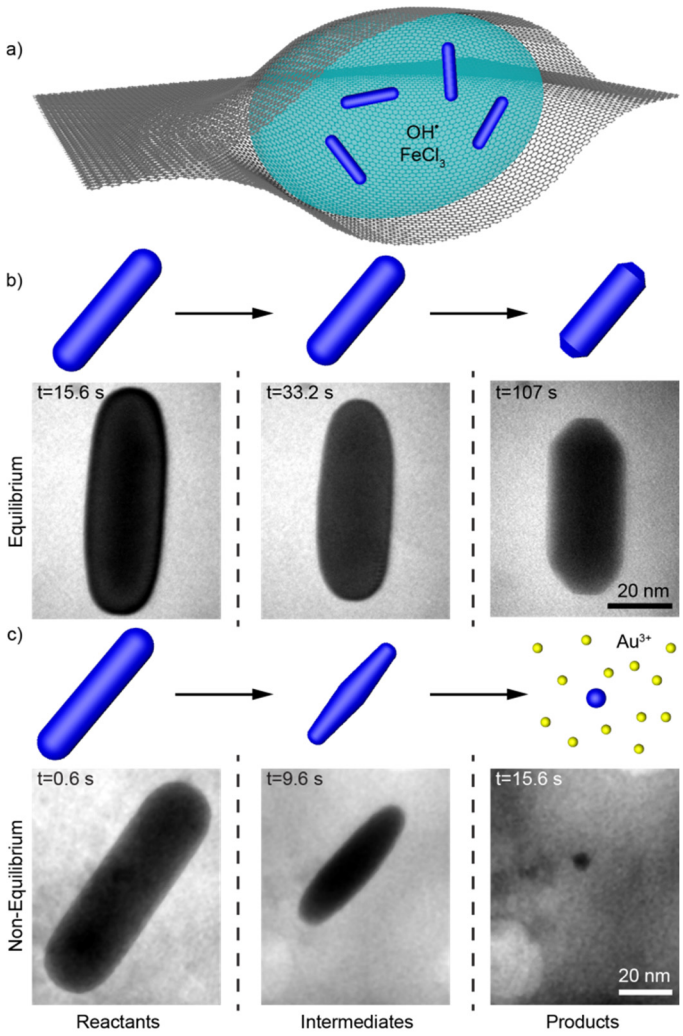

Figure 1. Real-time observation of near-equilibrium and non-equilibrium nanocrystal species in a graphene liquid cell. (a) Schematic liquid cell encapsulating a solution of gold nanocrystals. (b) Idealized reaction pathway and TEM images extracted from Movie S1 showing the reaction to generate near-equilibrium rods with flat {100} facets at the tips. (c) Idealized reaction pathway and TEM images extracted from Movie S2 showing the transition from rods to a non-equilibrium ellipsoidal intermediate with sharp tips.

The methods we employ to track nanocrystals as they are etched are illustrated first with a simple shape, rods (Fig. 1). At low $FeCl_3$ concentrations, reactions proceed slowly and show the development of low-energy facets (Fig. 1b, Movie S1, S9). In this scenario, the rate of etching is slow compared to the rate at which the particle is able to restructure and adopt a shape that is close to equilibrium.(*20*) At high $FeCl_3$ concentrations, however, fast reaction kinetics constantly drive the system out of equilibrium and the nanocrystal adopts a steady-state

ellipsoidal shape (Fig. 1c, Movie S2). It is important to note that previous ex-situ studies have investigated the etching of gold nanorods but have primarily observed tip-selective shortening.(*21*) The ellipsoidal intermediates are seen in our experiments because of our ability to capture the non-equilibrium steady-state products of the system.

The distinguishing feature of the non-equilibrium rod reaction is the change in the *relative* proportions of the particle through the development of tips that are sharper than the diameter, i.e. the formation of ellipsoids (Fig. 2a, Fig. S10, Movie S10). Analysis of the longitudinal dissolution rate and tip curvature changes over time show that periods during which the rod tips become sharper are well correlated with accelerated etching of the particle (Fig. 2b, Fig. S11). To better understand the spatiotemporal details of the reaction, we constructed time-domain contour plots: cross-sectional outlines of a changing nanocrystal extracted from frames that are equally spaced in time and colored based on calculation of the in-plane local curvature (Fig. 2c, Fig. S12-S13).(*22*) These data are consistent with the expectation that, because the rod tips are curved along two orthogonal dimensions while the sides are curved along one, the tips possess a lower areal ligand density and are therefore more chemically accessible and etch faster (Fig. S14);(*22-24*) this interpretation is supported by Monte Carlo simulations of rod etching (Fig. S15, Movie S11). Whereas in the near-equilibrium case, atoms at the tips have an opportunity to relax (e.g., via surface diffusion, Fig. S16, Movie S12),(*20, 23*) the persistent oxidative environment reacts with these species selectively, accelerating the reaction and driving the transient stabilization of the ellipsoidal intermediate. Etching reactions conducted on rods with synthetically blunted tips follow the same reaction trajectory (ellipsoidal intermediate), albeit with slower initial kinetics corresponding to selective removal of the blunt features (Fig. 2d-f, S12-S13, Movie S13-S14). Qualitatively similar dependencies on tip dimensionality and tip

curvature are observed for other nanocrystal shapes as well as when a rod and blunted rod pair are etched in the same field-of-view under identical conditions (Figs. S17-S18, Movies S15-S21).

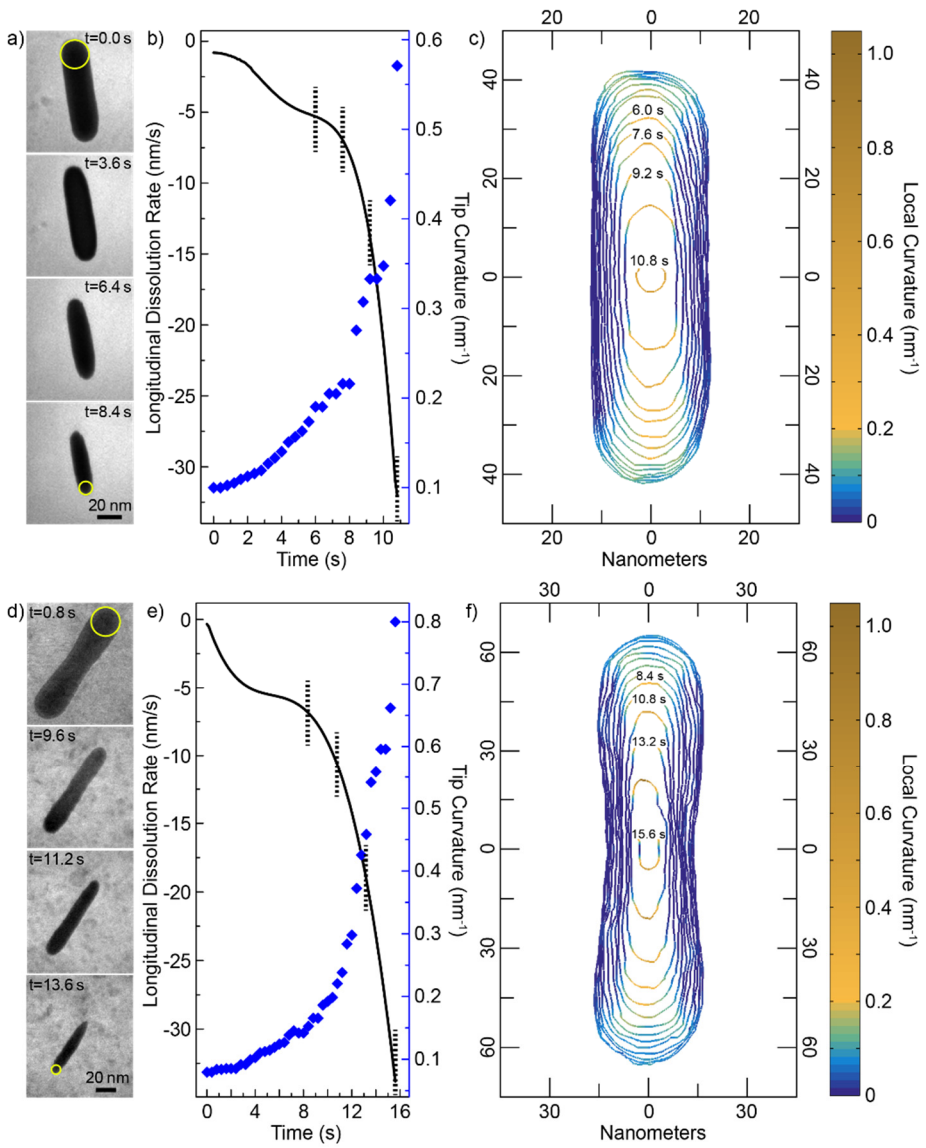

Figure 2. Sharp-tipped intermediates generated from the etching of pseudo-one-dimensional nanocrystals. Dissolution of a gold rod (a-c) and blunted rod (d-f) under non-equilibrium conditions. Selected time-lapse TEM images extracted from Movies S10 (a) and S13 (d), plots of longitudinal dissolution rate and tip curvature as a function of time (b, e), and time-domain contour plots (c, f). Yellow circles in (a, d) highlight the extrema of cross-sectional tip curvature. Vertical dotted lines in (b, e) correspond to the time-labeled contours in (c, f). Contour lines are spaced in time by 0.8 seconds in (c) and (f).

The etching of pseudo-one-dimensional nanocrystals demonstrates that persistent and selective etching at high-energy local features drives the formation of metastable intermediate

shapes. However, because for this class of particles the surface faceting is not easily characterized or agreed upon in the literature,(*25*) deducing a more detailed, atomistic understanding of non-equilibrium reactions is challenging. To address this, single-crystalline polyhedral nanocrystals with unambiguous surface faceting were subjected to the oxidative environment in the liquid cell and were observed to transition through *crystallographically well-defined* intermediate shapes.

We first describe results for a {100}-faceted cube (Movie S22-S23). The square cross-section indicative of the ⟨100⟩ zone axis of a cube is observed to transition through a faceted intermediate before adopting an isotropic shape and being oxidized completely (Fig. 3a, b). To determine a crystallographic assignment for the newly-developed intermediate shape, the angles between candidate {hkl} crystal facets viewed along the ⟨100⟩ zone axis were calculated and compared to those measured in the TEM images (Fig. 3c, d). This analysis reveals a transformation to high-energy {310} facets, indicative of a tetrahexahedron (THH)-shaped nanocrystal as the longest-lived intermediate.(*26, 27*)

We observe a similar shape transformation in Monte Carlo simulations of a schematic kinetic model for nanocrystal etching (Fig. 3b, d, Movies S24-S25). Here we take Au atoms to reside on sites of an FCC lattice and adopt rate constants $k(n)$ for etching of surface-exposed atoms that depend only on their coordination number, n. Despite its simplicity, this model produces a THH intermediate for a broad range of parameter values (Fig. S19). This non-equilibrium structure is unlikely to be a consequence of the electron beam, the particular oxidation chemistry employed in the liquid cell, or the presence of surface-bound ligands, as these effects are not explicitly considered in the simulation. When the driving force for oxidation is reduced in experiments, cubes transform into truncated octahedra (Fig. S20, Movie S26-

S27),(*28*) the expected equilibrium Wulff shape for an FCC lattice (Fig. S21).(*20, 23*). This same equilibrium transformation is observed in simulations when mechanisms of surface relaxation are introduced (Fig. S19, S22, Movies S28-S30, see SI for discussion).

Because the particles do not rotate significantly throughout the etching reaction, the crystallographic zone axis is constant and can be known beforehand via the cross-sectional appearance of the initial nanocrystals. This allows for the quantification of dissolution rates along specific [uvw] directions from time-domain contour maps (Fig. 3e, f, Fig. S23-S25). These data represent an experimental manifestation of the so-called Kinetic Wulff Construction,(*23*) but provide additional insight since they allow one to extract the time-dependence of crystallographic dissolution rates (Fig. 3e, Fig. S26). The ⟨110⟩ edges of the cubic nanocrystal exhibit the fastest initial etching rates, revealing the {310} THH facets which then experience a period of transient metastability (region II, Fig 3e) before all rates accelerate at small particle sizes (region III, Fig. 3e, f).

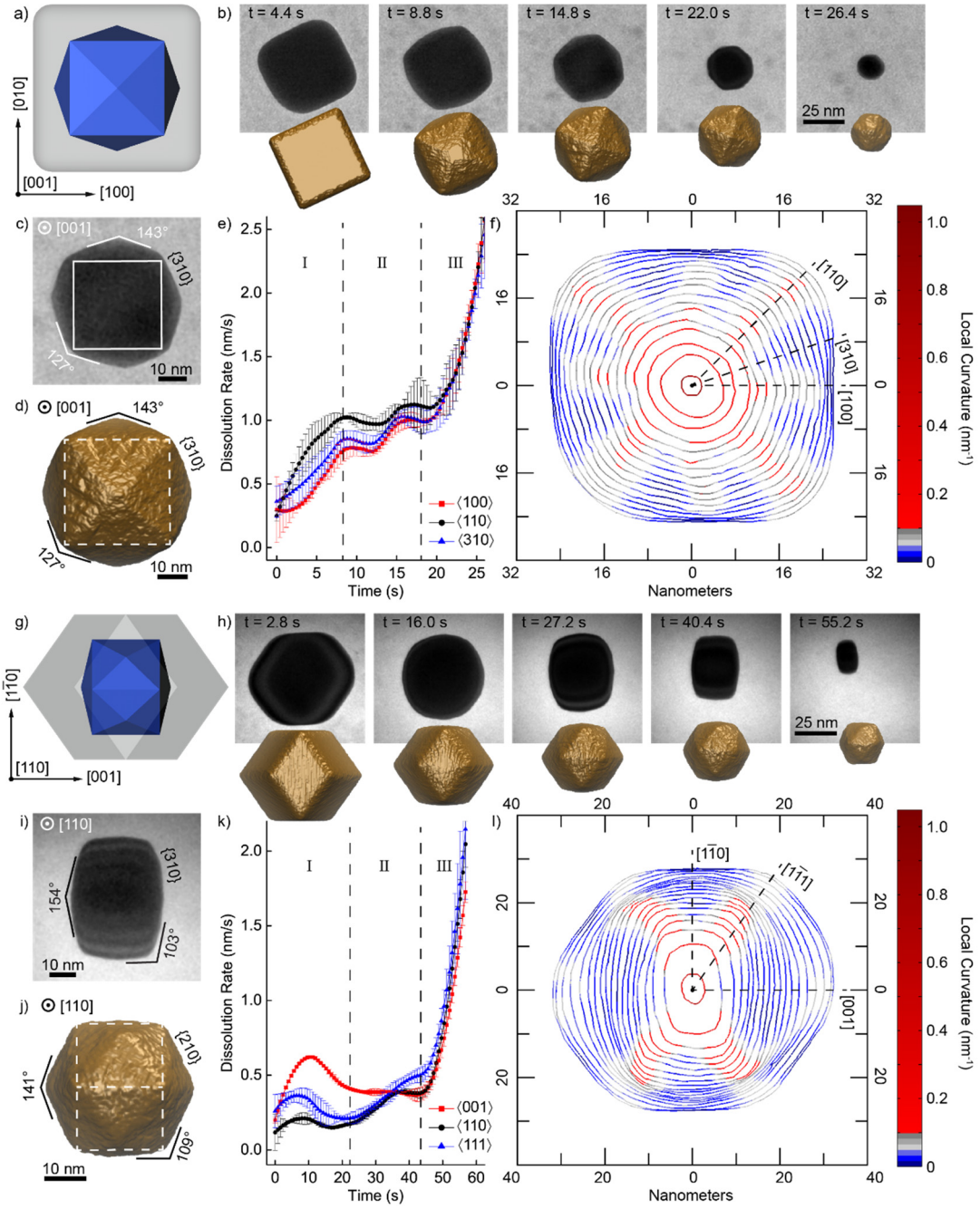

Figure 3. Crystallographically well-defined intermediates generated from polyhedral nanocrystals. Transition of a cube (a-f) and rhombic dodecahedron (g-l) to a tetrahexahedron during non-equilibrium etching. (a,g) Model of a crystallographically-oriented particle (grey) with intermediate tetrahexahedra shown internally (blue). (b, h) Time-lapse TEM images and corresponding snapshots from Monte Carlo simulations extracted from Movies S22, S24 (b) and S32, S34 (h). Tetrahexahedron intermediates with labeled zone-axis and calculated {hk0} facet angles are shown for the cube (c,d) and rhombic dodecahedron (i,j) reactions for experiment (c,i) and simulation (d,j). (e, k) Crystallographic dissolution rates extracted from contour plots, averaged over several symmetric directions. (f, l) Time-domain contour plots with relevant crystallographic directions labeled as dotted lines. Contour lines are spaced in time by 1.6 seconds in (f) and (l).

The formation of a well-defined THH intermediate is driven primarily by a coordination number (n)-dependent etching process (see SI for discussion). When the rate of deletion of surface atoms with $n = 6$ is much slower than surface relaxation, the equilibrium truncated octahedron is observed (Fig. S19, Movies S29-S30). However, when the rate of removal of surface atoms with $n = 6$ is faster than both surface relaxation and the removal of $n \geq 7$ atoms, the non-equilibrium THH intermediate is observed (Fig. 3b, d, Fig. S19, Movies S29-S30). This occurs through the lateral recession of sequential {100} layers via etching of the peripheral edge atoms which tend to have $n \leq 6$ (Fig. 4a, Fig. S27, Movie S31). This results in the gradual transition from {100} facets on the initial cube to a series of vicinal {hk0} facets and is corroborated by measurement of the facet h-index in both experiment and simulation (Fig. 4b). Because vicinal {hk0} facets consist of a series of {100} terraces ($n = 8$) separated by steps ($n = 6$) (Fig. 4c, d), continued removal of $n = 6$ atoms eventually results in a non-equilibrium steady-state condition where a series of stepped terraces are receding via their edges at a constant rate, resulting in the transient existence of the THH intermediate (Fig. 4e). We refer to this mechanism as step-recession. The reverse of this process, known as step-flow,(*29, 30*) occurs in many examples of crystal growth and serves as a foundation for continuum models of nanoparticle shape development (e.g. Kinetic Wulff Construction) and modern thin film fabrication techniques (e.g. Molecular Beam Epitaxy).(*23, 30*)

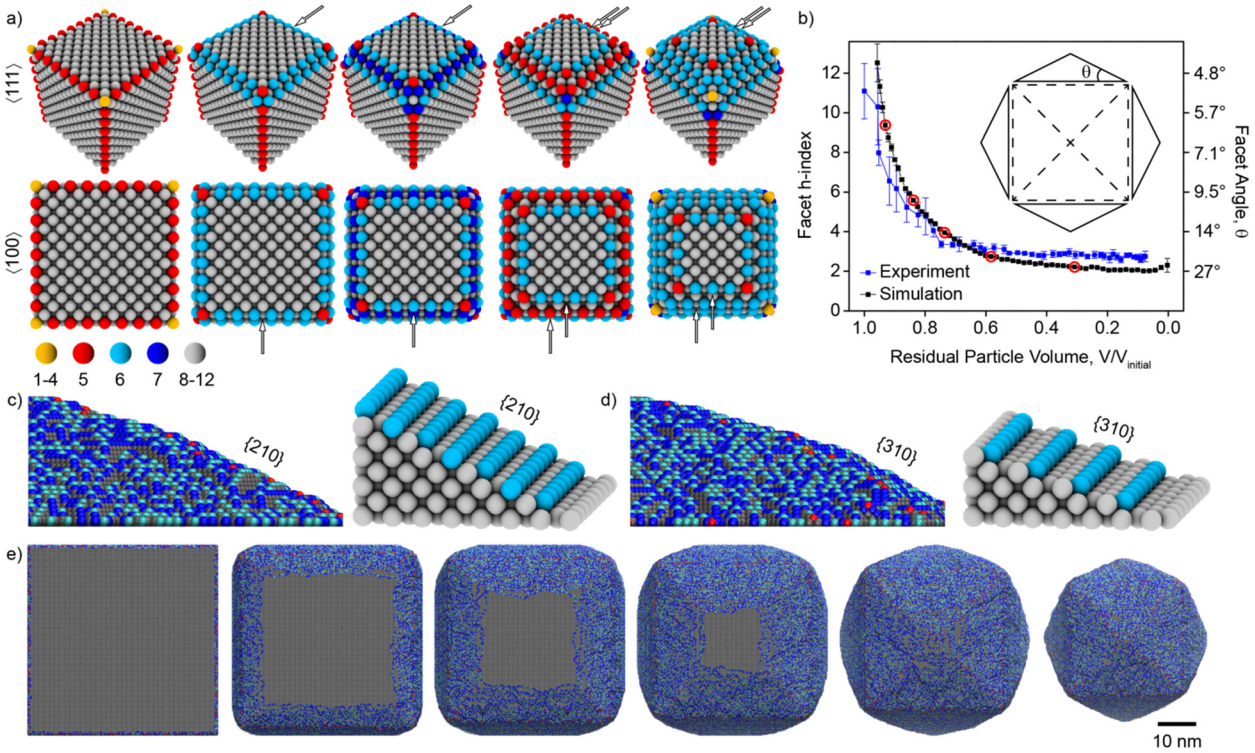

Figure 4. Coordination number and step-recession-based formation mechanism of intermediate nanocrystals. (a) Idealized etching of a cubic nanocrystal shown from two crystallographic perspectives wherein atoms with coordination number (n) ≤ 6 are deterministically removed at each step (Movie S31). Arrows denote the presence of {100} terraces that recede via removal of atoms at their step edges. Color-coded legend for n is shown at bottom left. (b) Time evolution of the vicinal facet effective h-index via measurement of the facet angle in both experiment and simulation (Movies S22, S24). Red circles correspond to the snapshots in part (e). (c,d) Simulation snapshot (left) and perfect model facet (right) of {210} (c) and {310} (d) facets. (e) Simulation snapshots of the progression of a cube to a steady-state non-equilibrium THH with atoms color-coded according to coordination number (Movie S25).

To determine the generality of these observations, single-crystalline rhombic dodecahedron (RD) nanocrystals were etched under similar conditions (Fig. 3g-l, Movies S32-S35). Indeed, the elongated hexagonal projection of the RD is observed to transition through a THH intermediate (viewed edge-on as a result of the ⟨110⟩ zone axis) before being oxidized completely (Fig. 3g, h). Although the experimental results show a {310} THH as the final kinetic product, simulations show a {210} THH (Fig. 3i, j, Fig. S28, Movies S36-S39), suggesting that additional factors that are not considered in simulations (e.g. CTAB binding to the larger {100} terrace area of {310} facets, Fig. 4c, d) may be important in dictating the precise facet morphology. (A similar discrepancy between the experiment and simulations for tip-selective

nanorod etching supports the idea that ligand binding can modulate relative facet stability; see above, Fig. S15, Movie S11). Nonetheless, the qualitative observation of a period of transient metastability of a THH intermediate is confirmed and can be quantified through similar Kinetic Wulff Construction and time-domain contour plot analysis techniques (Fig. 3k, l, Fig. S23-S26). The appearance of THH intermediates is also observed from a rhombic dodecahedron and cube pair, etched in the same field-of-view under identical conditions (Movie S40).

Our results suggest that the formation of a THH nanocrystal is a general property of FCC metal nanocrystals under a broad range of conditions that favor kinetic products. This may explain the observation that the synthetic nanocrystal literature contains a preponderance of reports of structures bounded by {hk0} rather than other, ostensibly equally likely, {hkl} facets.(*26, 27*) Additional nanocrystal shapes exhibited driving-force-dependent near-equilibrium and non-equilibrium transformation pathways, highlighting the generality of the observations described above (Fig. S29, Movies S41-44).

In the chemistry of atoms and molecules, the study of reactive intermediates is key to understanding molecular reaction mechanisms, and new tools for observing such intermediates are constantly sought. An analogy is often made between nanocrystals and artificial atoms and molecules. Here we have shown that liquid cell TEM provides for ready observation and mechanistic understanding of transient intermediates in the formation of nanostructures at the relevant time and length scales. This will add to our rapidly developing ability to create and control artificial nanoscale building blocks with high precision.

References:

1. H. Zheng, R. K. Smith, Y.-W. Jun, C. Kisielowski, U. Dahmen, A. P. Alivisatos, *Science* **324**, 1309-1312 (2009).
2. D. H. Son, S. M. Hughes, Y. Yin, A. Paul Alivisatos, *Science* **306**, 1009-1012 (2004).
3. Y. Sun, Y. Xia, *Science* **298**, 2176-2179 (2002).
4. S. H. Tolbert, A. P. Alivisatos, *Science* **265**, 373-376 (1994).
5. P. Buffat, J. P. Borel, *Phys. Rev. A* **13**, 2287-2298 (1976).
6. M. J. Mulvihill, X. Y. Ling, J. Henzie, P. Yang, *J. Am. Chem. Soc.* **132**, 268-274 (2010).
7. M. N. O'Brien, M. R. Jones, K. A. Brown, C. A. Mirkin, *J. Am. Chem. Soc.* **136**, 7603-7606 (2014).
8. M. J. Williamson, R. M. Tromp, P. M. Vereecken, R. Hull, F. M. Ross, *Nat. Mater.* **2**, 532-536 (2003).
9. N. de Jonge, F. M. Ross, *Nat. Nanotechnol.* **6**, 695-704 (2011).
10. D. Li, M. H. Nielsen, J. R. I. Lee, C. Frandsen, J. F. Banfield, J. J. De Yoreo, *Science* **336**, 1014-1018 (2012).
11. E. Sutter, K. Jungjohann, S. Bliznakov, A. Courty, E. Maisonhaute, S. Tenney, P. Sutter, *Nat. Commun.* **5**, (2014).
12. Q. Chen, H. Cho, K. Manthiram, M. Yoshida, X. Ye, A. P. Alivisatos, *ACS Cent. Sci.* **1**, 33-39 (2015).
13. J. Wu, W. Gao, J. Wen, D. J. Miller, P. Lu, J.-M. Zuo, H. Yang, *Nano Lett.* **15**, 2711-2715 (2015).
14. F. M. Ross, *Science* **350**, aaa9886 (2015).
15. J. M. Yuk, J. Park, P. Ercius, K. Kim, D. J. Hellebusch, M. F. Crommie, J. Y. Lee, A. Zettl, A. P. Alivisatos, *Science* **336**, 61-64 (2012).
16. J. Park, H. Elmlund, P. Ercius, J. M. Yuk, D. T. Limmer, Q. Chen, K. Kim, S. H. Han, D. A. Weitz, A. Zettl, A. P. Alivisatos, *Science* **349**, 290-295 (2015).
17. T. J. Woehl, J. E. Evans, I. Arslan, W. D. Ristenpart, N. D. Browning, *ACS Nano* **6**, 8599-8610 (2012).
18. H.-G. Liao, D. Zherebetskyy, H. Xin, C. Czarnik, P. Ercius, H. Elmlund, M. Pan, L.-W. Wang, H. Zheng, *Science* **345**, 916-919 (2014).
19. N. M. Schneider, M. M. Norton, B. J. Mendel, J. M. Grogan, F. M. Ross, H. H. Bau, *J. Phys. Chem. C* **118**, 22373-22382 (2014).
20. Y. Xia, X. Xia, H.-C. Peng, *J. Am. Chem. Soc.* **137**, 7947-7966 (2015).
21. C.-K. Tsung, X. Kou, Q. Shi, J. Zhang, M. H. Yeung, J. Wang, G. D. Stucky, *J. Am. Chem. Soc.* **128**, 5352-5353 (2006).
22. D. Alpay, L. Peng, L. D. Marks, *J. Phys. Chem. C* **119**, 21018-21023 (2015).
23. L. D. Marks, L. Peng, *J. Phys.: Condens. Matter* **28**, 053001 (2016).
24. Z. Nie, D. Fava, E. Kumacheva, S. Zou, G. C. Walker, M. Rubinstein, *Nat. Mater.* **6**, 609-614 (2007).
25. B. Goris, S. Bals, W. Van den Broek, E. Carbó-Argibay, S. Gómez-Graña, L. M. Liz-Marzán, G. Van Tendeloo, *Nat. Mater.* **11**, 930-935 (2012).
26. X. Ye, Y. Gao, J. Chen, D. C. Reifsnyder, C. Zheng, C. B. Murray, *Nano Lett.* **13**, 2163-2171 (2013).
27. M. L. Personick, M. R. Langille, J. Zhang, C. A. Mirkin, *Nano Lett.* **11**, 3394-3398 (2011).

28. M. Liu, Y. Zheng, L. Zhang, L. Guo, Y. Xia, *J. Am. Chem. Soc.* **135**, 11752-11755 (2013).
29. W. K. Burton, N. Cabrera, F. C. Frank, *Philos. Trans. R. Soc. London, A* **243**, 299-358 (1951).
30. J. Krug, in *Multiscale Modeling in Epitaxial Growth,* A. Voigt, Ed. (Birkhäuser Basel, Basel, 2005), pp. 69-95.

Acknowledgments:

This work was supported in part by the King Abdulaziz City for Science and Technology (KACST), Kingdom of Saudi Arabia, which provided for nanocrystal synthesis; the Defense Threat Reduction Agency (DTRA) under Award HDTRA1-13-1-0035 which provided for nanocrystal etching, postdoctoral support, and TEM instrumentation; the NSF-BSF International Collaboration in Chemistry program, NSF Grant No. CHE-1416161 and the BSF Grant No. 2013/604 which provided for computational resources; and the Director, Office of Science, Office of Basic Energy Sciences, Materials Sciences and Engineering Division of the U.S. Department of Energy under Contract DE-AC02-05CH11231 within the sp2-bonded Materials Program (KC2207) which provided for graphene growth, cell fabrication, and student support. This work made use of facilities at the National Center for Electron Microscopy (NCEM), supported by the Office of Science, Office of Basic Energy Sciences, U.S. Department of Energy, under Contract No. DE-AC02-05CH11231. Q.C. was supported by a Miller fellowship from Miller Institute for Basic Research in Science at UC Berkeley. G.M.R. acknowledges the NSF for a Graduate Research Fellowship. M.R.J. acknowledges the Arnold and Mabel Beckman Foundation for a postdoctoral fellowship.

Supplementary Materials:

S1. Materials and Methods

S2. Figures S1-S29

S3. Supplementary Text

S4. Movies S1-S48

S5. Supplementary References

Supplementary Information

Title: Direct Mapping of the Evolution of Individual Nanocrystals Undergoing Highly Non-Equilibrium Chemical Transformations

Authors:

Xingchen Ye,[#,†] Matthew R. Jones,[#,†] Layne B. Frechette,[†] Qian Chen,[†,▽] Alexander S. Powers,[†] Peter Ercius,[¶] Gabriel Dunn,[‡] Grant M Rotskoff,[£] Son C. Nguyen,[†] Vivekananda P Adiga,[‡] A. Zettl,[‡,ǁ,§] Eran Rabani,[†,ǁ,ǂ] Phillip L. Geissler,[†] and A. Paul. Alivisatos[*,†,¥,ǁ,§]

Affiliations:

[†]Department of Chemistry, [▽]Miller Institute for Basic Research in Science, [‡]Department of Physics, [¥]Department of Materials Science and Engineering, [£]Biophysics Graduate Group, University of California, Berkeley, Berkeley CA 94720, United States

[ǁ]Materials Sciences Division, [¶]The Molecular Foundry, Lawrence Berkeley National Laboratory, Berkeley, California 94720, United States

[§]Kavli Energy NanoScience Institute, University of California Berkeley and Lawrence Berkeley National Lab, Berkeley, CA 94720, United States

[ǂ]The Sackler Center for Computational Molecular and Materials Science, Tel Aviv University, Tel Aviv 69978, Israel

[#]These authors contributed equally.

[*]To whom correspondence should be addressed.

E-mail: alivis@berkeley.edu

S1. Materials and Methods

Nomenclature: Here we use the terminology laid out in (*1*) where specific crystallographic planes and directions are denoted by parenthesis and square brackets, respectively (e.g. (100) plane and [110] direction) while families of planes and families of directions that are related by symmetry are denoted by curly brackets and angled brackets, respectively (e.g. {100} planes and ⟨110⟩ directions).

Nanocrystal synthesis. Gold nanorods,(*2, 3*) pentagonal bipyramids,(*4*) triangular prisms,(*5*) decahedra,(*5*) cubes,(*6*) rhombic dodecahedra,(*6*) and octahedra(*6*) were synthesized according to previously reported methods. Nanocrystals were cleaned by two rounds of centrifugation at 6000 rpm for 15 min and were finally dispersed in Milli-Q water (18.2 MΩ·cm) with a concentration characterized by an optical density (OD) of 5-8 at the peak of their plasmonic resonance.

Preparation of graphene-coated TEM grids. Single-layer graphene was grown on copper foil by chemical vapor deposition. Selective removal of graphene from one side of the copper foil was achieved using mild oxygen plasma treatment. Individual 300-mesh Quantifoil gold TEM grids (Structural Probe, Inc. Catalog number: 4230G-XA) were placed on top of a piece of graphene-covered copper foil with the amorphous carbon film side facing the graphene. 15 μL of isopropanol was then dropped onto the copper foil to wet the interface between the graphene and the amorphous carbon film of the TEM grid (as isopropanol evaporates, the graphene layer becomes bound to the Quantifoil TEM grid). Then, the copper foil with adhered TEM grids on top was floated on a 0.1 g/mL aqueous solution of sodium persulfate (Sigma Aldrich) to etch the underlying copper foil. These graphene-coated TEM grids were subsequently rinsed with deionized water three times to remove the residual etching solution, and were left dry in air for further use.

Encapsulation of solution samples in graphene liquid cells (GLCs). Two 50 mL aqueous solutions of 0.01 M Tris buffer (Fisher Scientific) and 0.1 M $FeCl_3$ (Sigma Aldrich) were prepared separately. 90 μL of hydrochloric acid (HCl, 37 wt. % in water, 12.1 M) was added to

the 50 mL of 0.1 M $FeCl_3$ solution to suppress the hydrolysis of $FeCl_3$. The pH of this acidified 0.1 M $FeCl_3$ stock solution was determined to be 0.65 ± 0.02 by measuring six independently prepared solutions with an Accumet pH meter (Fisher Scientific). For nanocrystal etching experiments, unless otherwise specified, 0.6 mL of the acidified 0.1 M $FeCl_3$ solution was mixed with 0.9 mL of 0.01 M Tris buffer solution, to which 15 μL of an aqueous solution of gold nanocrystals was added. This resulted in a final nanocrystal concentration of 0.05-0.08 OD and a final pH of 0.92 ± 0.02 in the solution intended for encapsulation in graphene liquid cells. For experiments with different concentrations of $FeCl_3$, a certain volume of 0.1 M $FeCl_3$ solution was used and the volume of 0.01 M Tris buffer solution was adjusted accordingly to maintain the total volume to be 1.5 mL. In some control experiments, isopropanol was deliberately introduced to a final concentration of 0.15 M, as it is a known scavenger of oxidative species.(*7, 8*) To encapsulate liquid samples in graphene liquid cells, one graphene-coated TEM grid was first laid onto a glass slide with the graphene side facing upwards. Next, a small droplet of the aforementioned nanocrystal-etchant-Tris buffer solution was placed onto the central region of the TEM gird. Then, another graphene-coated TEM grid was gently placed on top of the droplet, forming sealed graphene liquid pockets within 10 min. The sandwiched graphene liquid cell was loaded into a TEM for imaging within 30 min of its formation.

Electron microscopy and image analysis. TEM imaging was performed on a 200 kV Tecnai G2 20 S-TWIN TEM equipped with a Gatan Orius SC200 CCD camera. To measure electron dose rate, a TEM image was acquired under the same imaging conditions but with both sample and the objective aperture extracted. The electron dose rate was calculated from the total pixel intensity using the conversion ratio of 10 counts in the CCD camera as being equivalent to 1 electron.(*9*) The frame rate used for video acquisition was either 2.5 frames-per-second (fps) or 5.0 fps. High-resolution TEM imaging was performed using the 300 kV aberration-corrected TEAM I microscope at the National Center for Electron Microscopy facility within The Molecular Foundry at Lawrence Berkeley National Laboratory. The detector used was a Gatan K2-IS direct electron detector with 400 fps acquisition capability. Video processing and image analysis were accomplished using ImageJ, Adobe Photoshop, and home-written MATLAB codes utilizing built-in functions of the Image Processing Toolbox in Matlab.

Kinetic Model for Monte Carlo simulations.

Our model for nanocrystal etching resolves only the collection C of FCC lattice sites that are occupied by gold atoms at a given time. This list changes as a result of stochastic microscopic events whose rate constants we prescribe.

The dynamics of an atom detaching from the surface of a nanoparticle is shaped by many factors: the local surface structure, presence and arrangement of passivating ligand molecules, and the spatial distribution of oxidizing species, among others. We focus exclusively on the expectation that more highly coordinated atoms face higher energetic barriers to detachment, and are therefore etched less rapidly. Specifically, the removal rate $k(n)$ of a particular surface atom is taken to depend only on the number n of its nearest-neighbor lattice sites that are occupied.

Many features of the resulting etching trajectories are insensitive to the precise form of $k(n)$, requiring only that it declines sharply with n for highly coordinated sites. The particular form we choose follows from a simple kinetic description of the association between oxidizing species in solution and the nanoparticle surface: oxidants bind to a given surface atom with rate k_{on}; upon binding, a surface atom (denoted Au) becomes activated for etching (denoted Au^*). The activated surface atom may either deactivate (through unbinding of the oxidant, which occurs with rate k_{off}) or detach from the nanoparticle with rate k_{detach}, as represented in the chemical equation:

$$Au \underset{\leftarrow k_{off}}{\overset{k_{on}}{\rightarrow}} Au^* \xrightarrow{k_{detach}} 0. \tag{1}$$

The resulting rate of detachment, $r = k_{detach}p(Au^*)$, thus depends on the probability $p(Au^*)$ that the atom is activated. The quantity $p(Au^*)$ is generally time-dependent; for simplicity, we employ a steady-state approximation $\frac{dp(Au^*)}{dt} \approx 0$, which leads to:

$$k_{on}p(Au) - \left(k_{off} + k_{detach}\right)p(Au^*) \approx 0, \tag{2}$$

yielding an effective rate constant for etching $k = r/p(Au)$,

$$k = \frac{k_{on}}{1 + k_{off}/k_{detach}}. \tag{3}$$

Surface atoms that detach readily once activated (relative to the rate of oxidant unbinding) thus etch at essentially the same rate, i.e., etchant binding is the rate limiting step. Sites that detach slowly even when activated etch at much lower rates.

We take an Arrhenius form for detachment kinetics,

$$k_{detach} = k_0 e^{-\beta \epsilon n}, \tag{4}$$

with an energetic barrier that grows linearly with coordination number n, where $\beta = 1/k_B T$. Assuming k_{off} to be independent of n, and defining parameters μ and n^* through:

$$e^{\beta \mu} = \frac{k_{off}}{k_0} \tag{5}$$

$$\mu = -n^* \epsilon, \tag{6}$$

we finally have:

$$k = \frac{k_{on}}{1 + e^{\beta \epsilon (n - n^*)}} \tag{7}$$

or equivalently,

$$k = \frac{k_{on}}{1 + e^{\beta (\epsilon n + \mu)}}. \tag{8}$$

We anticipate that reaction barriers are high, $\beta \epsilon \gg 1$, so that the Fermi function form of Eq. (7) implies:

$$k(n) \approx k_{on}, \qquad n < n^* \tag{9}$$

$$k(n) \approx k_{on} e^{-\beta\epsilon(n-n^*)} \ll k_{on}, \qquad n > n^*. \tag{10}$$

The second expression for the effective etching rate, Eq. (8), highlights an isomorphism between our kinetic model and Monte Carlo sampling of a classic statistical mechanics model for phase separation, namely the lattice gas.(*10*)

We generated a collection of stochastic etching trajectories for several different values of n^* using the Gillespie algorithm for kinetic Monte Carlo sampling with the rates given in Eq. (7). We obtain essentially indistinguishable results using instead a discrete-time Monte Carlo scheme based on the aforementioned lattice gas analogy (an explicit comparison between these two methods for $n^* = 6.5$ is shown in Fig. S35.) The latter approach offers significant practical advantages when the model is elaborated to describe surface diffusion. For this reason, most of the trajectories we report were generated with lattice gas Monte Carlo methods, which we detail below. (Except where noted, results presented in all figures were generated in this way.)

Lattice gas Monte Carlo.

The dynamical variables of a lattice gas specify the presence ($\rho_i = 1$) or absence ($\rho_i = 0$) of material at each of a collection of lattice sites i. Their equilibrium fluctuations in a grand canonical ensemble are governed by a distribution of $C = \{\rho_1, \rho_2, \dots\}$ given by:

$$P(C) \propto e^{-\beta H}, \tag{11}$$

with the Hamiltonian:

$$H = -\mu \sum_i \rho_i - \epsilon \sum_{\langle i,j \rangle} \rho_i \rho_j, \tag{12}$$

where μ is an externally imposed chemical potential. The second summation in H includes all distinct pairs of nearest neighbor lattice sites, which contribute an attractive energy $-\epsilon$ when both are occupied.

The simplest Monte Carlo scheme for sampling the distribution Eq. (11) would (i) select a lattice site i at random, (ii) attempt to change its occupation state $\rho_i \rightarrow 1 - \rho_i$, and (iii) accept the change with probability $A(C \rightarrow C')$, where C and C' are the states of the system before and after

the proposed change. Any choice of A that satisfies detailed balance suffices for this purpose. The Glauber acceptance probability (*11*):

$$A(C \to C') = \frac{1}{1 + e^{\beta\left(H(C') - H(C)\right)}}, \tag{13}$$

is a common choice, particularly when trajectories are given a dynamical interpretation (associating a small time interval with each MC step). If the configurational distribution changes smoothly in time, then this discrete-time scheme is equivalent to a continuous-time kinetics with transition rates:

$$k(C \to C') = w_0 A(C \to C'), \tag{14}$$

where w_0 is a constant with units of inverse time. In the particular case of a deletion move, which takes $\rho_i = 1$ to $\rho_i = 0$, this rate becomes:

$$k(C \to C') = \frac{w_0}{1 + e^{\beta(\epsilon n + \mu)}}, \tag{15}$$

where n is the coordination number of site i in configuration C. This rate corresponds precisely to the etching rate $k(n)$ described in the previous section, establishing an equivalence between our kinetic model of nanocrystal etching and the deletion moves of a discrete-time grand canonical Glauber Monte Carlo sampling. In light of this equivalence, we interpret the chemical potential $\mu = -\epsilon n^*$ as a proxy for the driving force for etching. While it could be related in a complicated way to such underlying factors as etchant concentration and the electron beam strength, we treat it as an effective parameter that determines which coordination-number-dependent etching events are facile.

The precise lattice gas sampling scheme sketched above is not well-suited for etching trajectories, since only a small fraction of lattice sites are capable of changing in a given configuration (those at the nanocrystal surface). We therefore propose Monte Carlo moves that attempt only to modify the occupation state of changeable lattice sites. For deletion moves, the number of such changeable sites is $N_{surf}(C)$, i.e., the number of atoms that are incompletely coordinated. For insertion moves, the number of changeable sites is instead the number $N_{vac}(C)$ of vacancies that

are adjacent to occupied sites (though in the strongly non-equilibrium etching regime, the probabilities of insertion moves are so small that these moves are insignificant.)

Our primary scheme for simulating the etching of a nanoparticle is thus as follows:

1. Determine whether to attempt deleting an atom or inserting an atom, with probability $1/2$ for either move.

2. If attempting *insertion*, select one vacancy j at random from the $N_{vac}(C)$ vacancies associated with the configuration. Then, accept the "trial move" of changing the current configuration C into another configuration C' by changing $\rho_j = 0$ to $\rho_j = 1$ with probability:

$$A_{insert}(C \to C') = \frac{1}{1 + (f(C, C'))^{-1}}, \tag{16}$$

where:

$$f(C, C') = \frac{N_{vac}(C)}{N_{surf}(C')} e^{-\beta \Delta H}, \tag{17}$$

$$\Delta H = H(C') - H(C) = -\mu - \varepsilon n. \tag{18}$$

The ratio of N's in the function f preserves detailed balance, and $\beta = 1/k_B T$ is the inverse temperature.

If attempting *deletion*, select one atom j at random from the $N_{surf}(C)$ atoms associated with the configuration. Then, accept the trial move $C \to C'$ by changing $\rho_j = 1$ to $\rho_j = 0$ with probability:

$$A_{delete}(C \to C') = \frac{1}{1 + (g(C, C'))^{-1}}, \tag{19}$$

where:

$$g(C, C') = \frac{N_{surf}(C)}{N_{vac}(C')} e^{-\beta \Delta H}, \tag{20}$$

$$\Delta H = H(C') - H(C) = \mu + \varepsilon n. \quad (21)$$

The ratio of N's in the function g preserves detailed balance.

3. Repeat until the nanoparticle has been fully etched - i.e., no atoms remain.

Choice of parameters.

In all simulations, the temperature was set to $k_B T = k_B * 300K = 0.0259eV$, and the bond energy ε was set to $0.3275eV$, one-twelfth the bulk sublimation energy of gold.(*12*) THH intermediates were observed for a relatively wide range of chemical potentials, $-8 < \frac{\mu}{\varepsilon} < -6$. In the language of the kinetic model, this corresponds to etching rates for which $6 < n^* < 8$. At $\mu/\epsilon = -6$,[1] the FCC lattice gas exhibits coexistence between macroscopic high-density and low-density phases, so that the crystal surfaces can relax substantially on the time scale of growth or etching. We find that the equilibrium truncated octahedron emerges in etching simulations at a value of μ/ϵ slightly above coexistence, e.g. $\mu/\epsilon = -5.98$. For significantly larger values than this (around $\mu/\epsilon = -5.9$ and above), the shape evolution is instead dominated by growth of the nanoparticle. Precisely at $\mu/\epsilon = -6$, any *finite* initial structure constitutes a sub-critical nucleus, which dissolves as a consequence of interfacial tension on time scales that hinder surface relaxation.(*13*)

Surface relaxation.

In the lattice gas scheme described above, the equilibrium truncated octahedron shape is obtained only when the rate of insertion of atoms is approximately equal to the rate of deletion of atoms, which occurs within a narrow range of chemical potential. By contrast, in experiments the equilibrium shape is observed under a wider range of driving forces. This indicates that the dominant mechanism of surface relaxation may not be insertion moves as controlled by a chemical potential, but rather surface diffusion mediated by the etchant. (In the absence of oxidizing conditions, surface diffusion on a nanoparticle is very slow).(*14*) We therefore also performed simulations where we attempted to relax nanoparticles via such diffusion moves.

[1] For a general lattice, coexistence occurs at $\mu^* = -Z\epsilon/2$, where Z is the maximum number of nearest neighbors that a lattice site can have. For an FCC lattice, $Z = 12$, so $\mu^* = -6\epsilon$.

We considered three different types of diffusion moves: "local" diffusion moves, where a surface atom can hop to a nearest-neighbor vacancy; "global" diffusion moves, where a surface atom can move to any unoccupied surface site on the nanoparticle; and an intermediate type of move, where a surface atom can hop to a nearest-neighbor vacancy or a *second* nearest-neighbor vacancy. We call this last type of move a "2-local" move.

To execute a local or global diffusion move, a surface atom is selected at random and a vacancy (chosen in a way appropriate to the type of diffusion that is being used) is also selected at random. (2-local moves are chosen in a somewhat different manner, which will be explained separately). These trial moves are then accepted with probabilities that preserve detailed balance; for local moves the probability is:

$$A_{local}(C \to C') = \frac{1}{1 + (d_l(C, C'))^{-1}}, \tag{22}$$

where:

$$d_l(C, C') = \frac{N_{surf}(C) n_{vac}(i)}{N_{surf}(C') n_{vac}(j)} e^{-\beta \Delta E}, \tag{23}$$

$$\Delta E = E(C', j) - E(C, i) = -\epsilon_{diff} \Delta n. \tag{24}$$

Here, $n_{vac}(i)$ is the number of vacancies adjacent to atom i of configuration C, ϵ_{diff} is the energy barrier to diffusion, and Δn is the total change in the number of bonds in going from C to C'. The ratio of N's and n's in d_l is chosen so as to preserve detailed balance. For global moves, the probability is:

$$A_{global}(C \to C') = \frac{1}{1 + (d_g(C, C'))^{-1}}, \tag{25}$$

where:

$$d_g(C, C') = \frac{N_{surf}(C) N_{vac}(C)}{N_{surf}(C') N_{vac}(C')} e^{-\beta \Delta E}, \tag{26}$$

$$\Delta E = E(C') - E(C) = -\epsilon_{diff} \Delta n. \tag{27}$$

Here Δn is again the total change in the number of bonds and the ratio of N's and n's in d_g is chosen so as to satisfy detailed balance.

For 2-local moves, surface atoms are still selected at random, but the vacancies are selected slightly differently. In particular, instead of selecting a single vacancy from a list of all eligible vacancies, one of the nearest neighbors of the selected atom is chosen at random (regardless of whether that neighbor is occupied or unoccupied), and then a neighbor of *that* site is chosen at random (again, regardless of whether that neighbor is occupied or unoccupied.) Then, this site is rejected if it is not a surface vacancy, i.e. a vacancy that is a nearest neighbor of a surface atom.[2] If the site *is* a surface vacancy, then the diffusion move is accepted with a probability:

$$A_{2-local}(C \to C') = \frac{1}{1 + (d_{2l}(C, C'))^{-1}}, \tag{28}$$

where:

$$d_{2l}(C, C') = \frac{N_{surf}(C)}{N_{surf}(C')} e^{-\beta \Delta E}, \tag{29}$$

$$\Delta E = E(C') - E(C) = -\epsilon_{diff} \Delta n. \tag{30}$$

Calculation of h-index from Monte Carlo simulations. We used simple geometry to calculate the h-index in our simulations. The "h" refers to the first index in the general zone-axis formula {hkl}, and represents (the inverse of) the slope of a series of receding {100} surfaces, i.e. the inverse of the slope of the pyramidal faces in our simulated THH nanoparticles. To compute h, the value of the h-index, consider the vectors $\vec{v}_{100}$ and $\vec{v}_{110}$, which point from the center of a THH nanoparticle to the border of the nanoparticle in the [100] and [110] directions, respectively. Define the *difference* between these vectors as the *h-vector*:

$$\vec{v}_h = \vec{v}_{100} - \vec{v}_{110}$$

These vectors are shown in the figure below. With respect to a coordinate system with $\hat{v}_{100} = \vec{v}_{100}/|\vec{v}_{100}|$ fixed, the slope of h-vector is given by:

[2] For a given atom in an FCC lattice, there are thus 12x12=144 ways to select a (1st- or 2nd- nearest neighbor) site. Many of these sites will not be surface vacancies, of course, and so a number of them will be rejected; we found this approach simpler than explicitly finding and listing all the 1st- and 2nd- nearest neighbor surface vacancies.

$$m = \frac{\vec{v}_h \cdot \hat{v}_{100}}{\vec{v}_h \cdot (\mathbf{1} - \hat{v}_{100}\hat{v}_{100})}$$

Where $\mathbf{1}$ is the 3×3 unit matrix and $\hat{v}_{100}\hat{v}_{100}$ is the dyad formed from $\hat{v}_{100}$. The h-index is calculated as the inverse of the slope of the h-vector:

$$h = 1/m$$

In our calculations, for each configuration, the h-index is computed by averaging over the 24 possible h-indices of the THH (6 pyramids × 4 faces on each pyramid.)

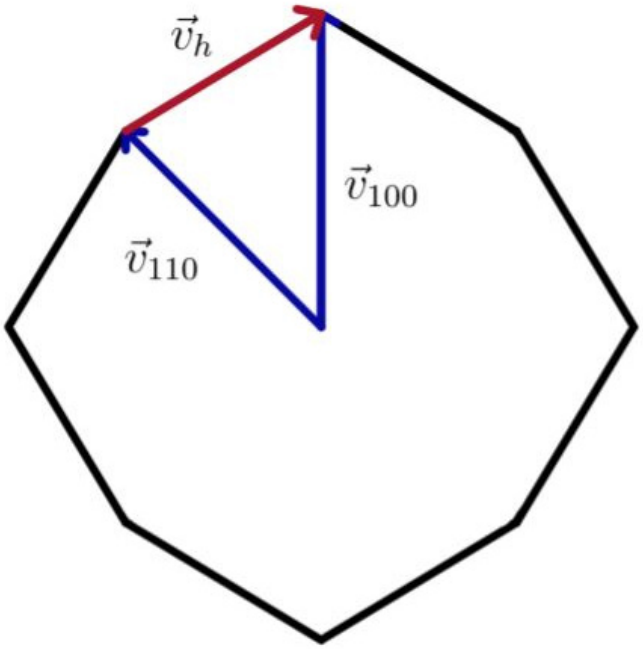

S2. Supplementary Figures

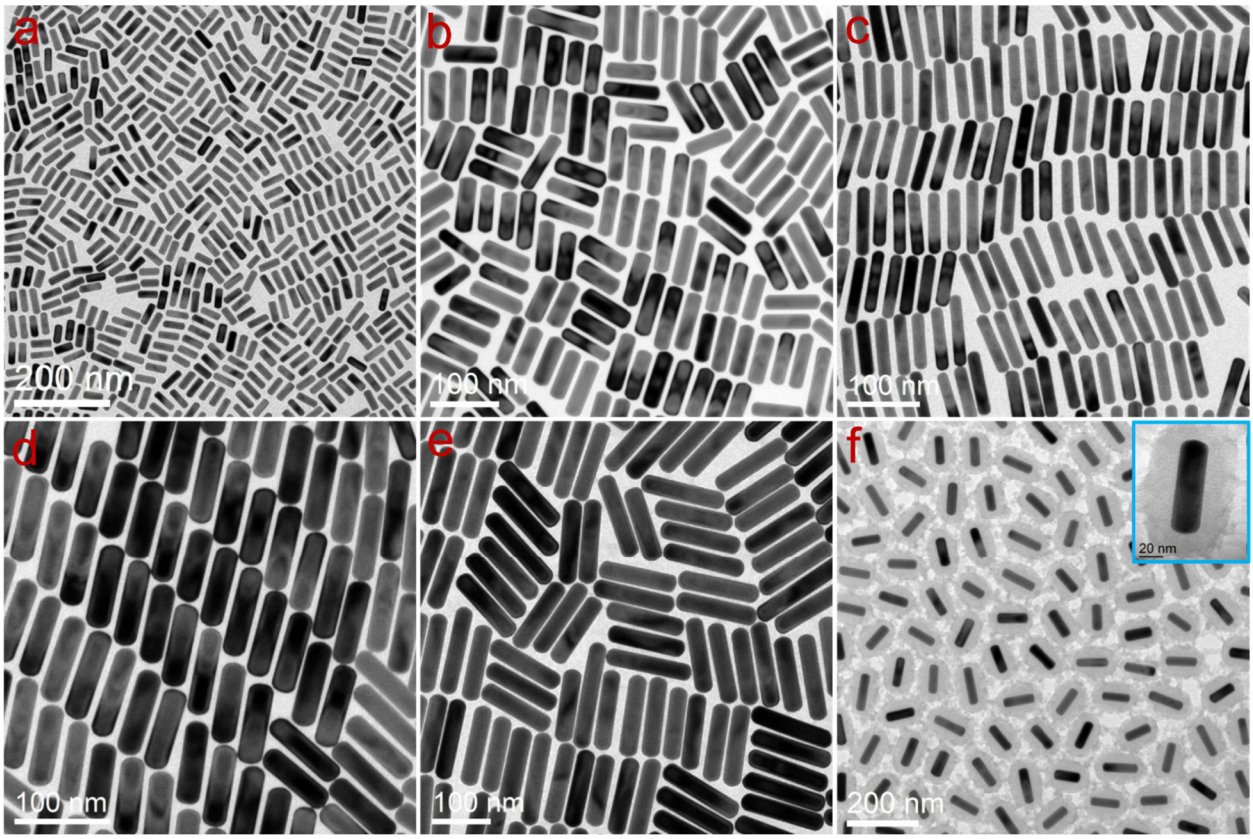

Figure S1. TEM images of different gold nanorod (a-e) and silica-coated gold nanorod (f) samples. The average dimensions are: (a) (46.5 ± 3.4) nm × (15.1 ± 1.0) nm, (b) (75.0 ± 3.5) nm × (25.2 ± 1.9) nm, (c) (84.1 ± 4.8) nm × (17.6 ± 1.5) nm, (d) (90.1 ± 4.0) nm × (24.2 ± 1.7) nm, (e) (140.5 ± 7.4) nm × (32.0 ± 2.0) nm, (f) (78.0 ± 4.8) nm × (23.5 ± 1.0) nm. Silica shell thickness: 25.3 ± 1.0 nm.

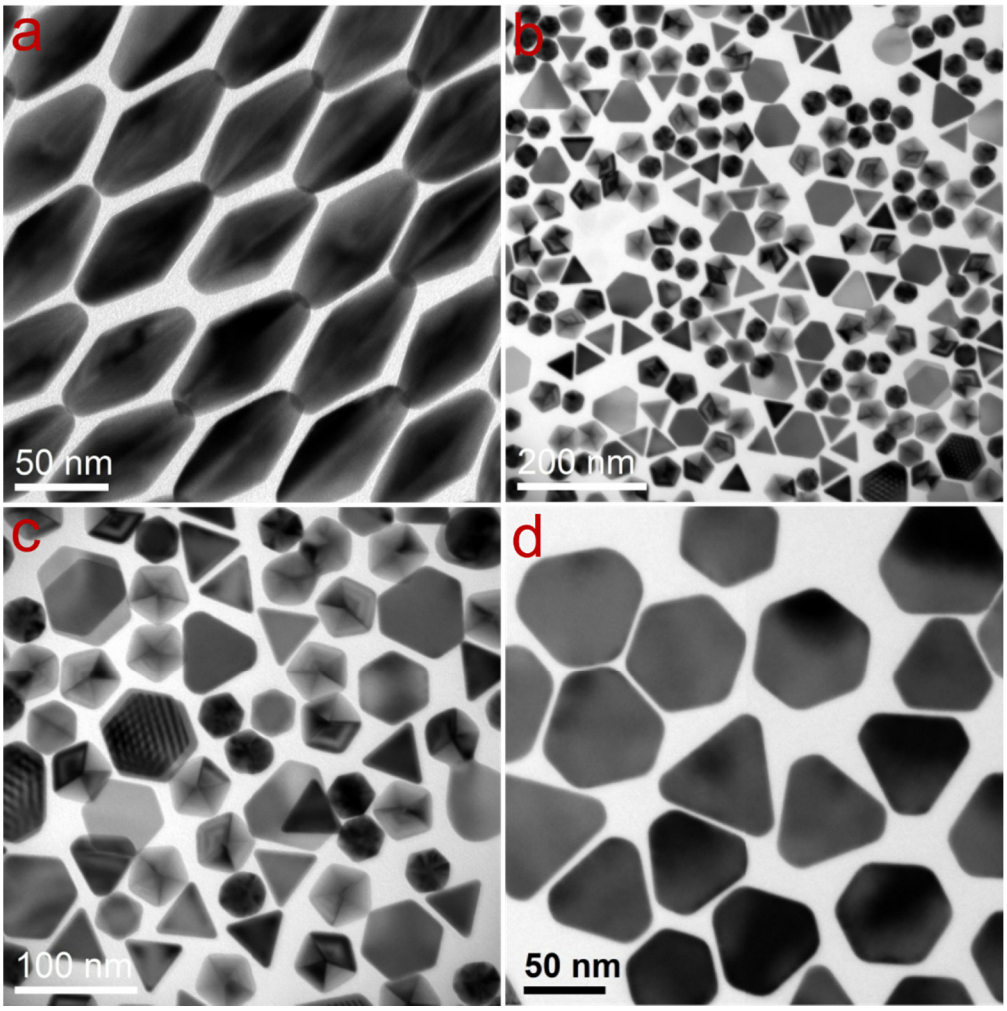

Figure S2. TEM images of gold pentagonal bipyramid (a) and prism (b-d) samples. As shown in (b-d), the as-synthesized prism sample is composed of a mixture of hexagonal prisms, triangular prisms, icosahedra, and decahedra.

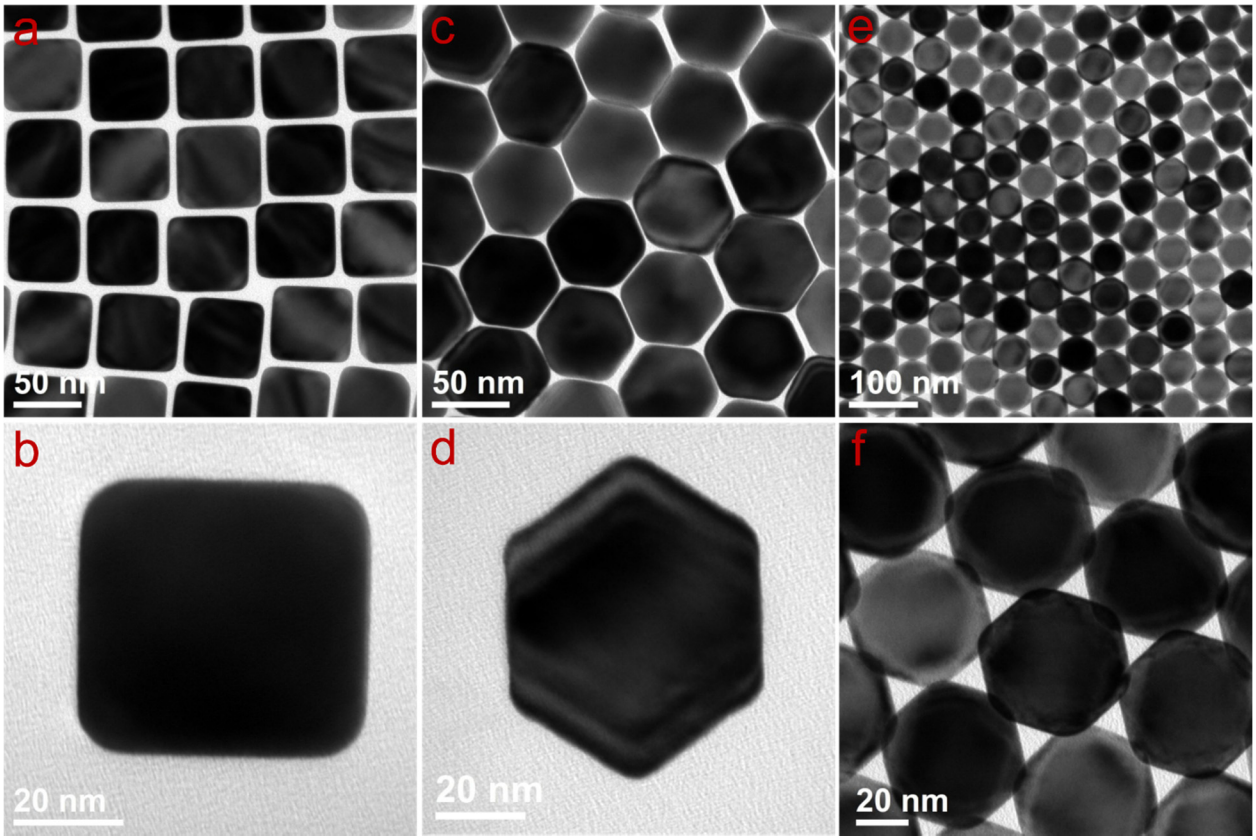

Figure S3. TEM images of gold cubes (a,b), rhombic dodecahedra (c,d), and octahedra (e,f).

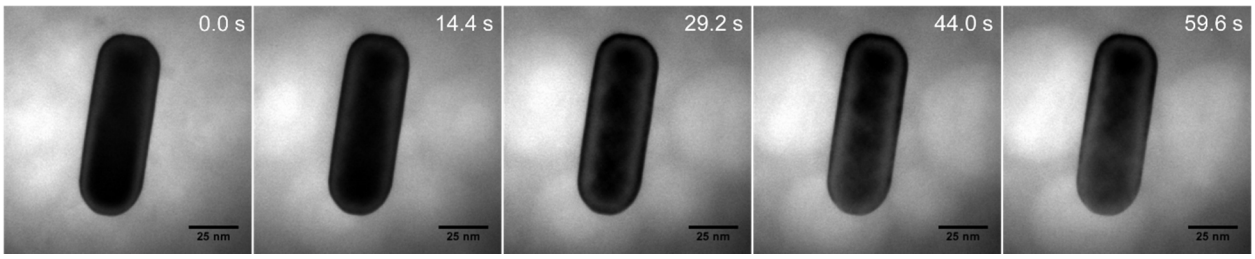

Figure S4. Sequential images extracted from Movie S3. No etching was observed when a solution of gold nanorods dispersed in Tris buffer (pH=8.2) was encapsulated in a GLC without $FeCl_3$. The electron dose rate was 217 electrons/$Å^2$·s.

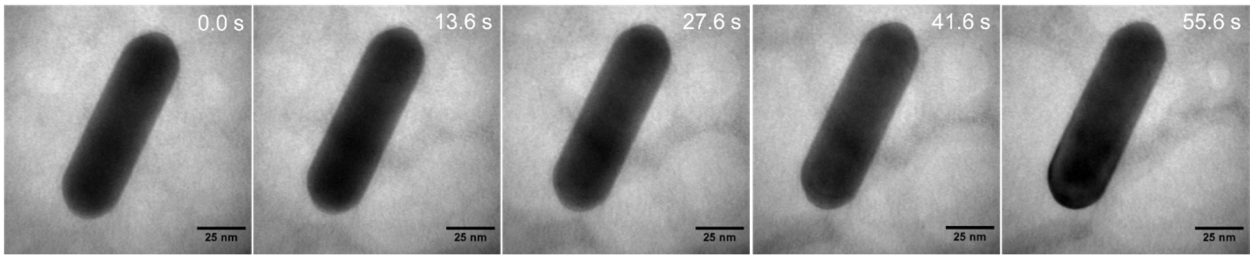

Figure S5. Sequential images extracted from Movie S4. No etching was observed when an acidic solution (acidified with HCl, pH=0.92) of gold nanorods dispersed in Tris buffer was encapsulated in a GLC without $FeCl_3$. The electron dose rate was 217 electrons/$Å^2$·s.

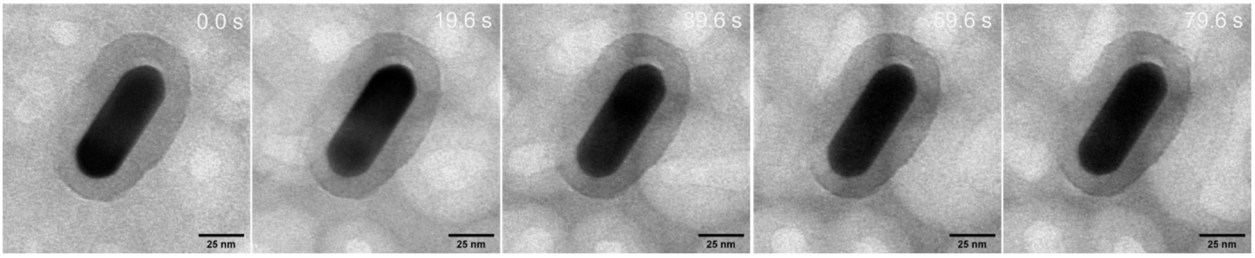

Figure S6. Sequential images extracted from Movie S5. No etching was observed when a solution of Au@SiO_2 nanorods dispersed in a mixture of Tris buffer and acidified $FeCl_3$ was encapsulated in a GLC (final [$FeCl_3$] =0.04 M, pH=0.92). The electron dose rate was 217 electrons/$Å^2$·s.

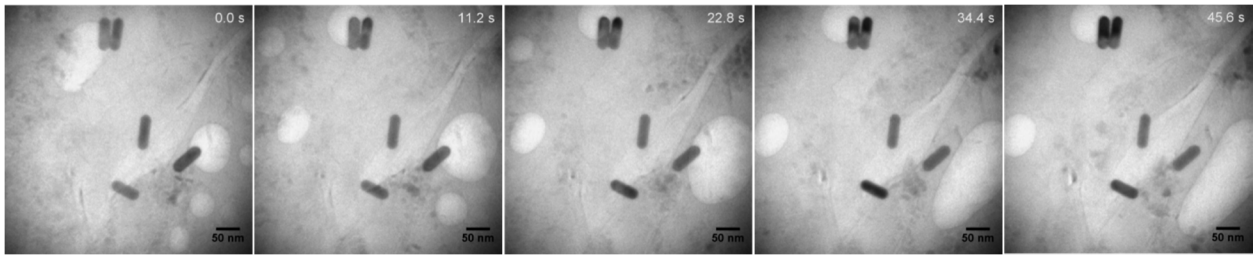

Figure S7. Sequential images extracted from Movie S6. No etching was observed when a solution of Au nanorods dispersed in a mixture of Tris buffer, acidified $FeCl_3$, and isopropanol to quench oxidative species was encapsulated in a GLC (final [$FeCl_3$] =0.04 M, [isopropanol] =0.15M, pH=0.92). The electron dose rate was 86 electrons/$Å^2$·s.

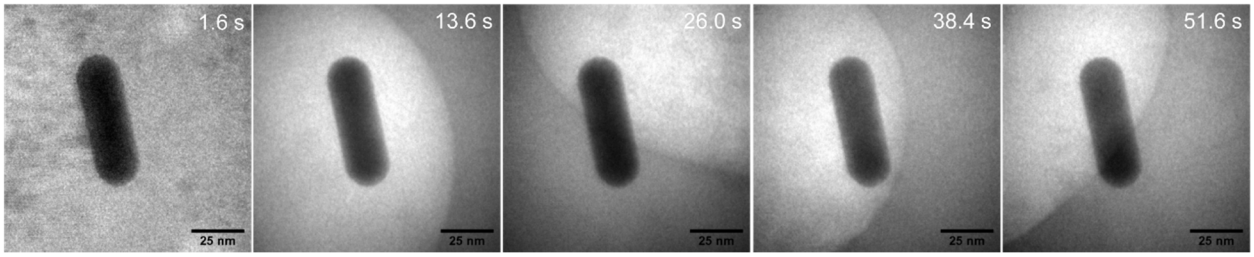

Figure S8. Sequential images extracted from Movie S7. No etching was observed when a solution of Au nanorods dispersed in a mixture of Tris buffer, acidified $FeCl_3$ and isopropanol to quench oxidative species was encapsulated in a GLC (final [$FeCl_3$] =0.04 M, [isopropanol] =0.15M, pH=0.92). The electron dose rate was 254 electrons/$Å^2$·s.

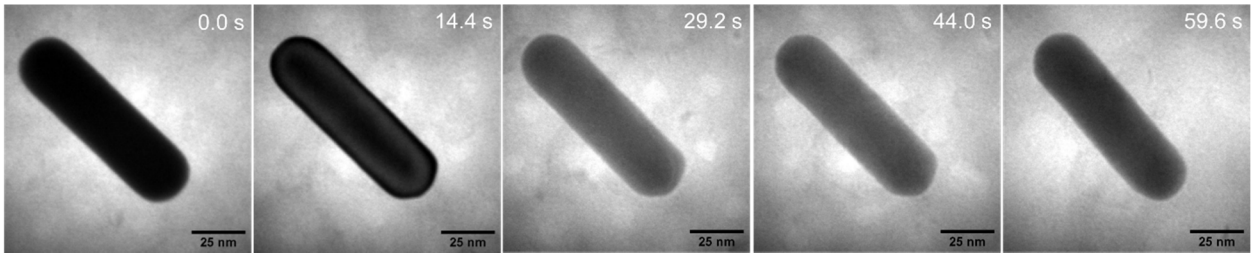

Figure S9. Sequential images extracted from Movie S8. A negligible degree of etching was observed when a solution of Au nanorods dispersed in a mixture of Tris buffer and a lower concentration of acidified $FeCl_3$ was encapsulated in a GLC (final [$FeCl_3$] =0.02 M, pH=1.25). The electron dose rate was 217 electrons/$Å^2$·s.

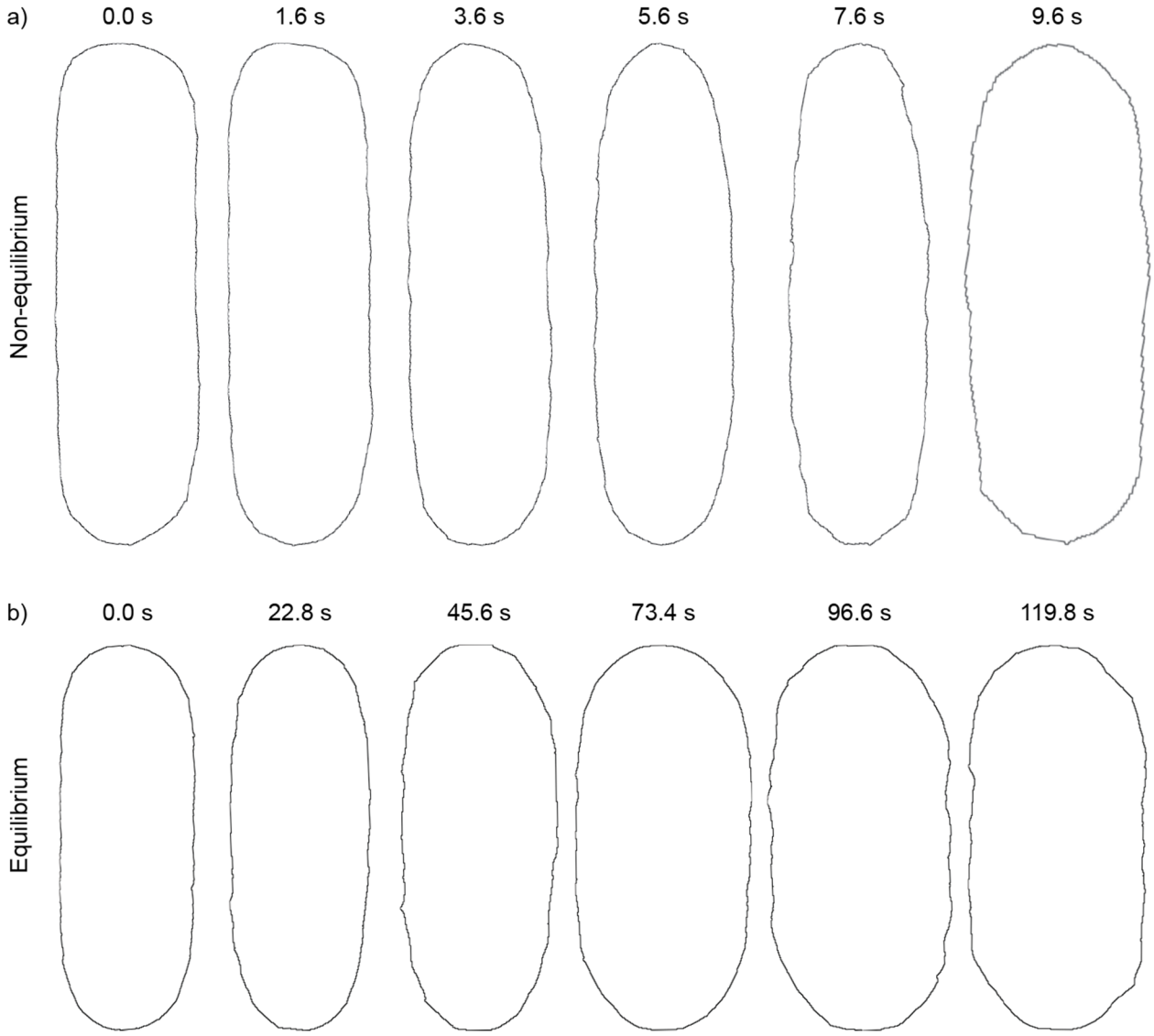

Figure S10. Selected contours of rod etching reactions under fast kinetic (a, Movie S10) and slow equilibrium (b, Movie S1) conditions that have been scaled to better illustrate the change in *relative* particle shape. Contrast the appearance of an ellipsoidal intermediate in the non-equilibrium regime with the blunting and faceting observed in the equilibrium regime.

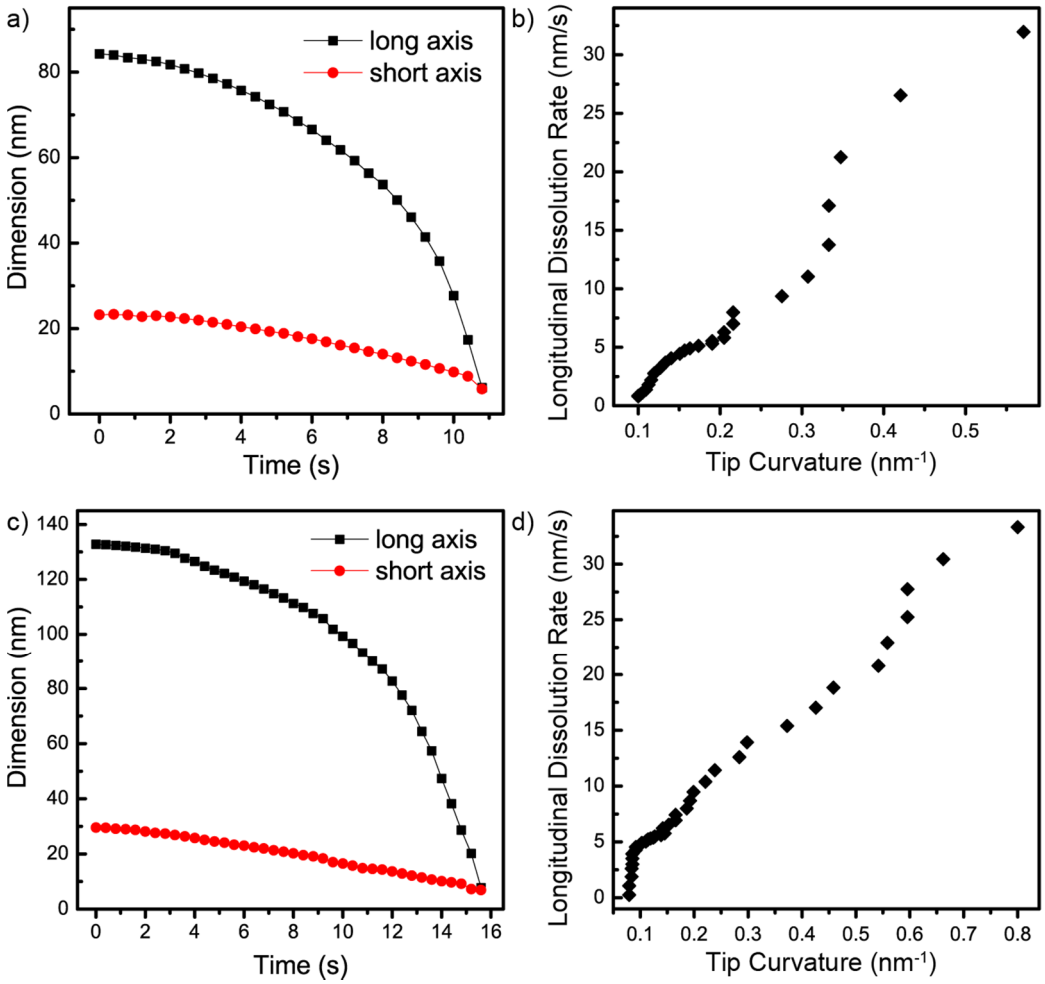

Figure S11. Plots of dimensions versus time (a,c) and longitudinal dissolution rate versus tip curvature (b,d) for the rod (a,b) and blunted rod (c,d) shown in Figure 2. The electron dose rate was 217 electrons/Å^2·s.

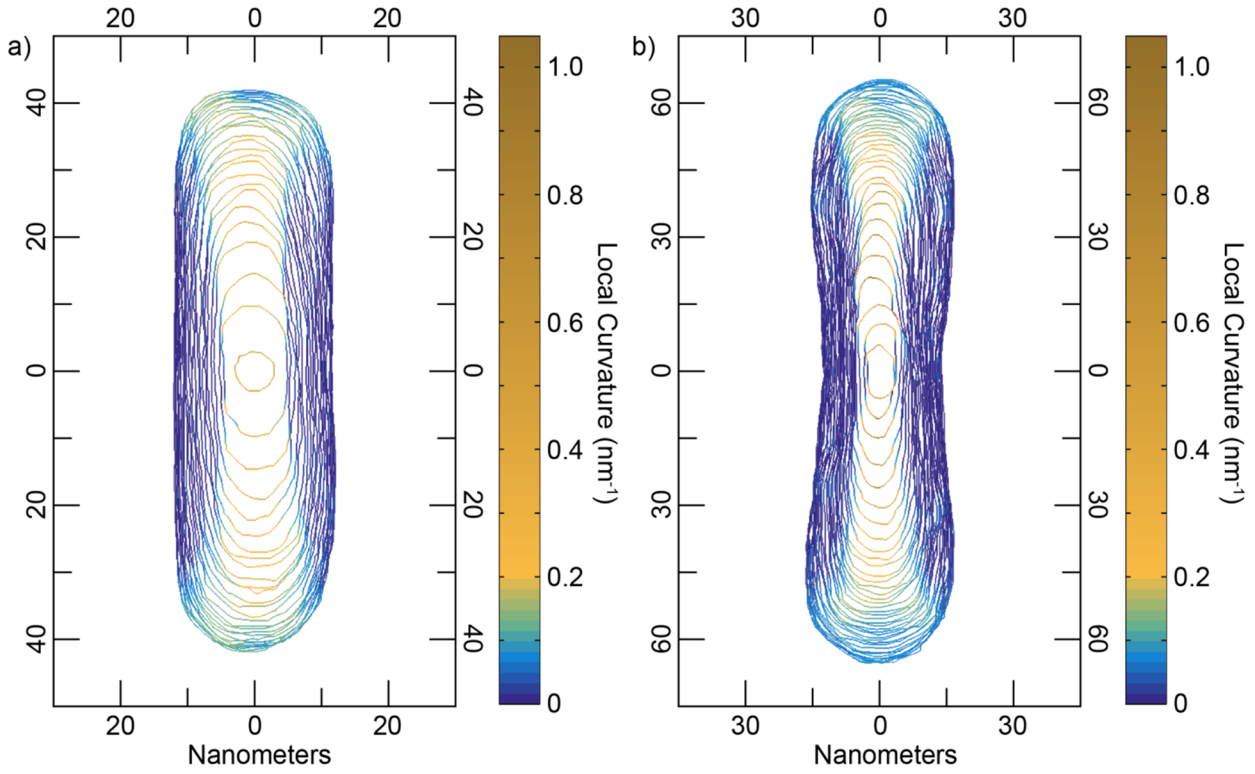

Figure S12. Complete dataset of time-domain contour plots for the rod (a) and blunted rod (b) reactions shown in Figure 2. Contour lines are spaced in time by 0.4 seconds.

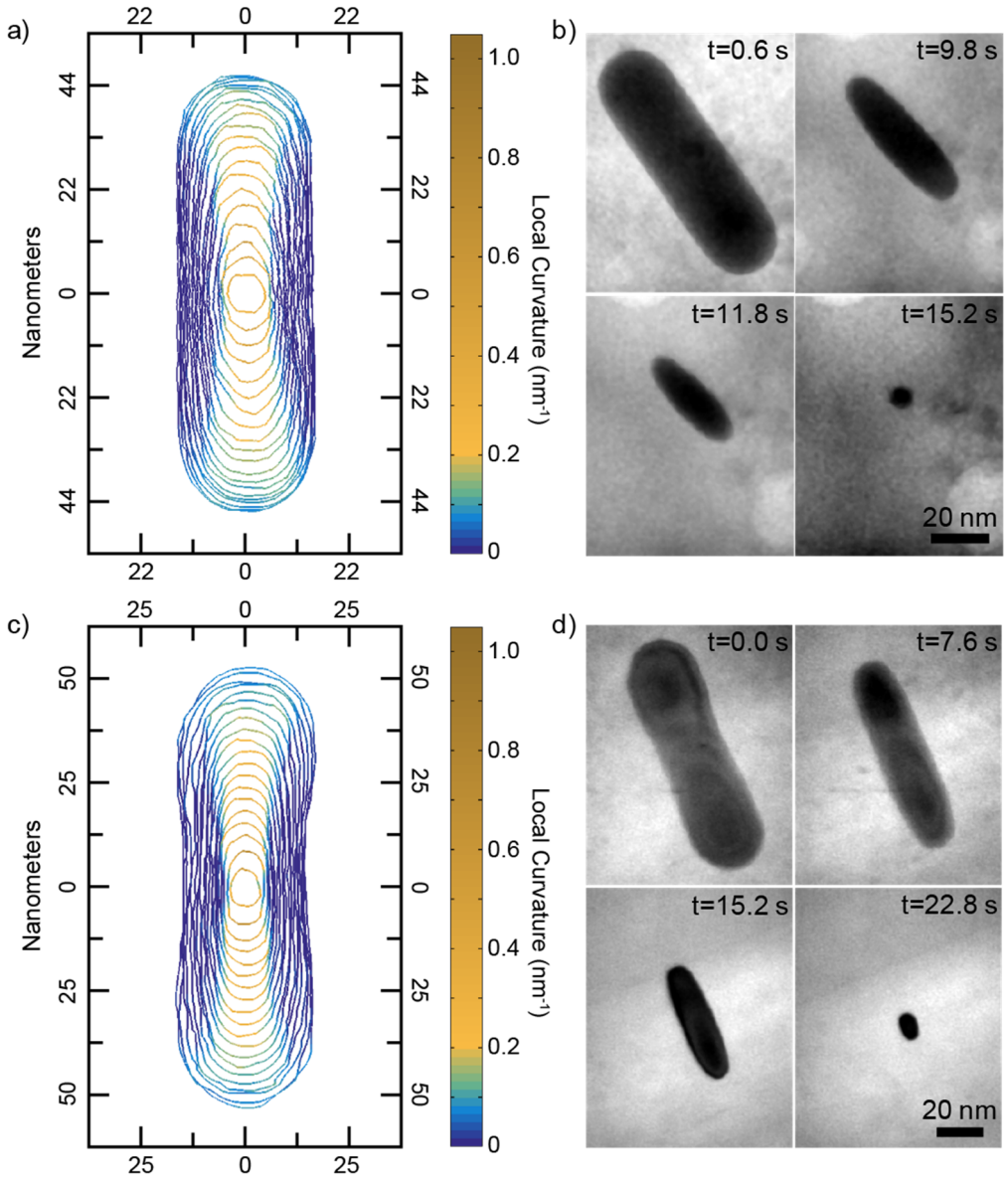

Figure S13. Time-domain contour plots and selected time-lapse TEM images of additional oxidative dissolution reactions for gold rod (a,b) and blunted rod (c,d) nanocrystals extracted from Movies S2 (a,b) and S14 (c,d), respectively. Contour lines are spaced in time by 0.8 and 1.2 seconds in (a) and (c), respectively. The electron dose rate was 217 electrons/Å^2·s.

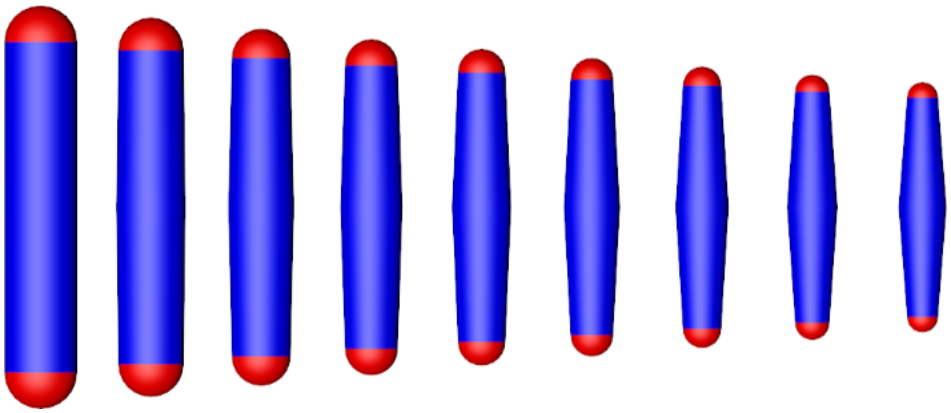

Figure S14. Schematic illustrating how curvature-selective etching can result in sharper-tipped nanocrystal intermediates. Because the tips of nanorods (red hemispheres) are curved along two orthogonal dimensions but the sides of nanorods (blue cylinders) are curved along one dimension, a lower areal density of surface ligands is expected at the tips than the sides. This results in more rapid removal of material at the tips relative to the sides, generating an ellipsoidal geometry. For example, when schematic nanorod tips (red) are reduced by 10% while the sides (blue) are reduced by 5% over several steps (left to right sequence of images), a sharper-tipped ellipsoidal nanocrystal intermediate is generated. Presumably, under normal solution conditions, surface relaxation would equilibrate these high-energy features, resulting in the shortened but still rod-shaped nanocrystals that have been frequently observed in *ex situ* experiments. The sustained non-equilibrium conditions in the liquid cell allow observation of the ellipsoidal intermediate by ensuring that the rate of atom removal is faster than the rate of surface relaxation.

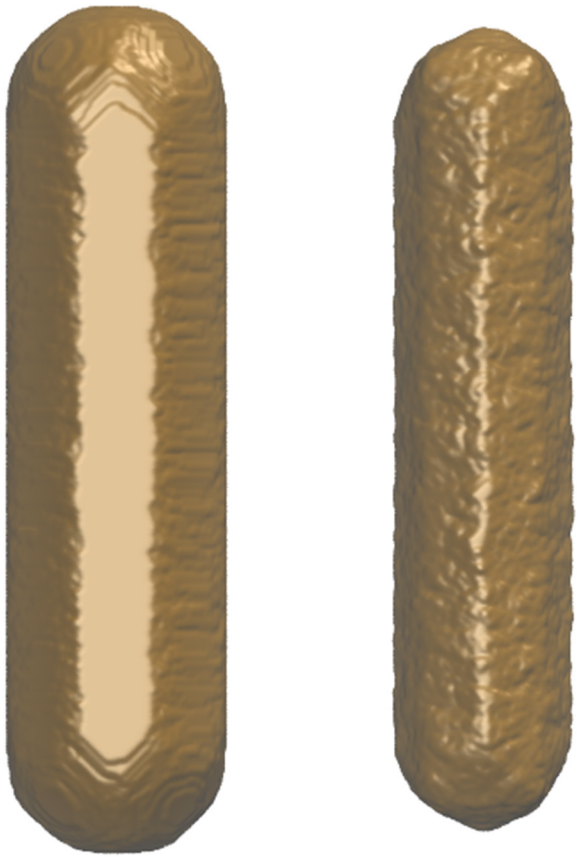

Figure S15. Comparison of rod etching simulations under near-equilibrium (left, $\frac{\mu}{\epsilon} = -5.98$) and non-equilibrium (right, $\frac{\mu}{\epsilon} = -6.5$) conditions (Movie S11). For the near-equilibrium rod etching, the number of attempted steps was 5.00×10^7 and the acceptance ratio was ~0.0317. For the non-equilibrium rod etching, the number of attempted steps was ~3.00×10^7 and the acceptance ratio was ~0.0677. Images are viewed along the ⟨100⟩ zone axis. Whereas the experimental faceting of the rod under near-equilibrium conditions (Fig. S10, S16, Movie S1) is observed in the simulation (left), the experimental tip-selective etching and transformation to an ellipsoidal intermediate (Fig. S10, S12, S13, Movie S2) is not observed in the simulation (right). This implies that the effects of decreased areal ligand density around the nanorod tips (which are not considered in the simulation) are responsible for the experimental observations. As mentioned in the main text, this interpretation is consistent with numerous reports from the literature.(*15, 16*)

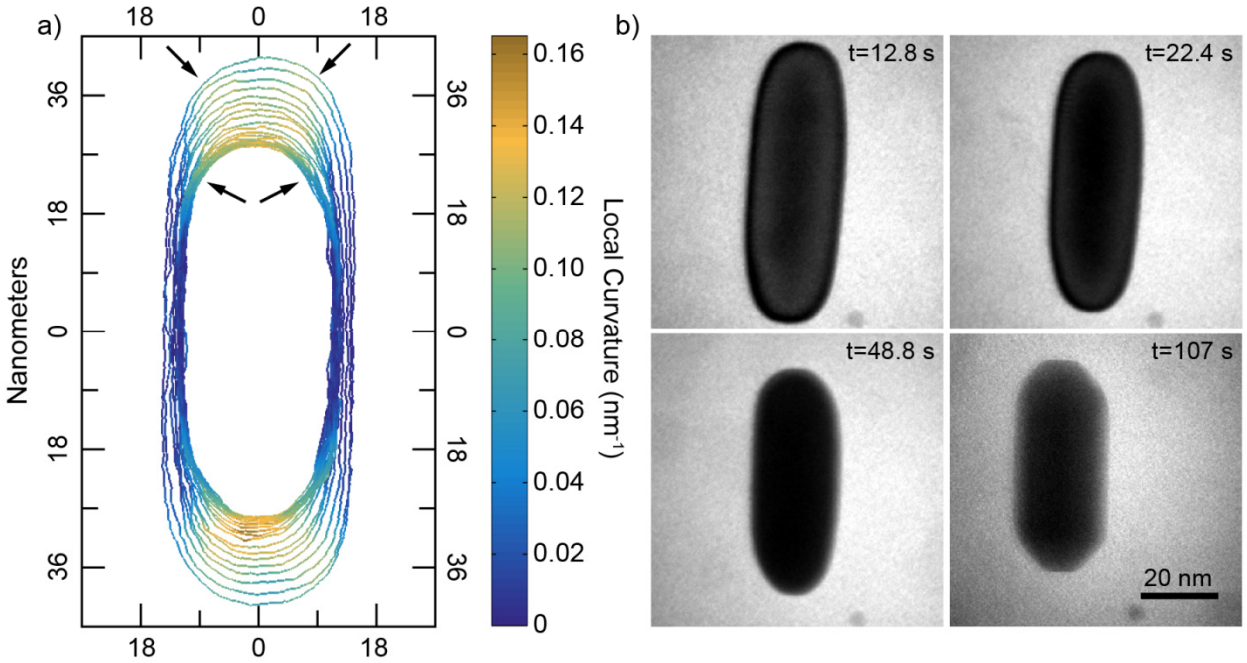

Figure S16. Time-domain contour plot (a) and selected time-lapse TEM images (b) for the equilibrium rod dissolution reaction shown in Figure 1 extracted from Movie S1. Note the initial appearance of sharp features (top set of arrows) which eventually develop into lower-energy blunt facets (bottom set of arrows, see Movie S12 for further illustration). Contour lines are spaced in time by 3.6 seconds. The electron dose rate was 217 electrons/Å^2·s.

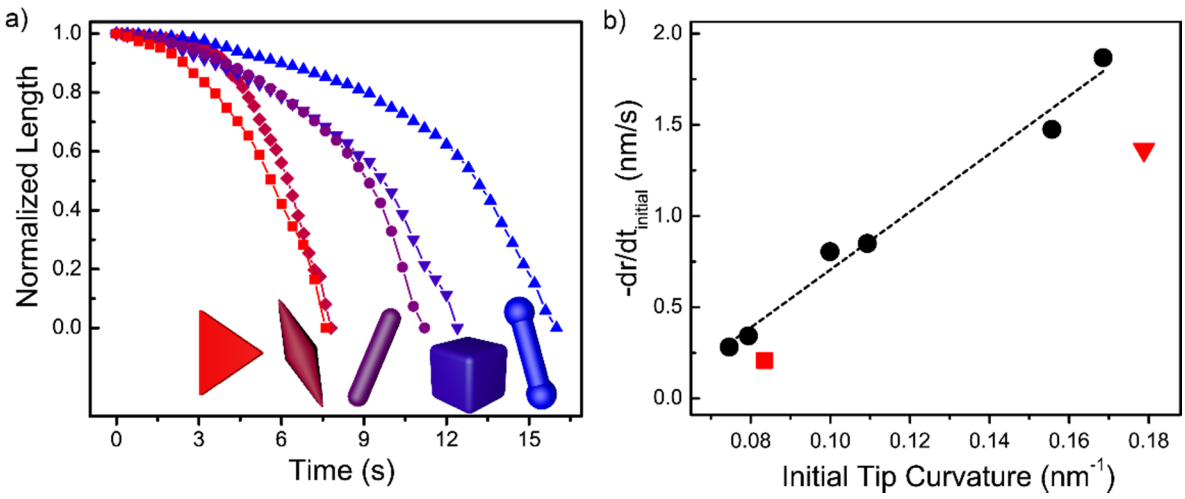

Figure S17. (a) Normalized length versus time for several different nanocrystal shapes extracted from Movies S20 (triangular prism), S15 (pentagonal bipyramid), S10 (rod), S48 (cube), and S14 (blunted rod). (b) Quantification of the initial etching rate as a function of initial tip curvature for differently-sized rods and bipyramids (black), and for a cube (red square) and a triangular prism (red triangle). Note the deviation from the linear trend for the particles with curvature along only one dimension (red data points) compared to those with curvature along two orthogonal dimensions (black data points).

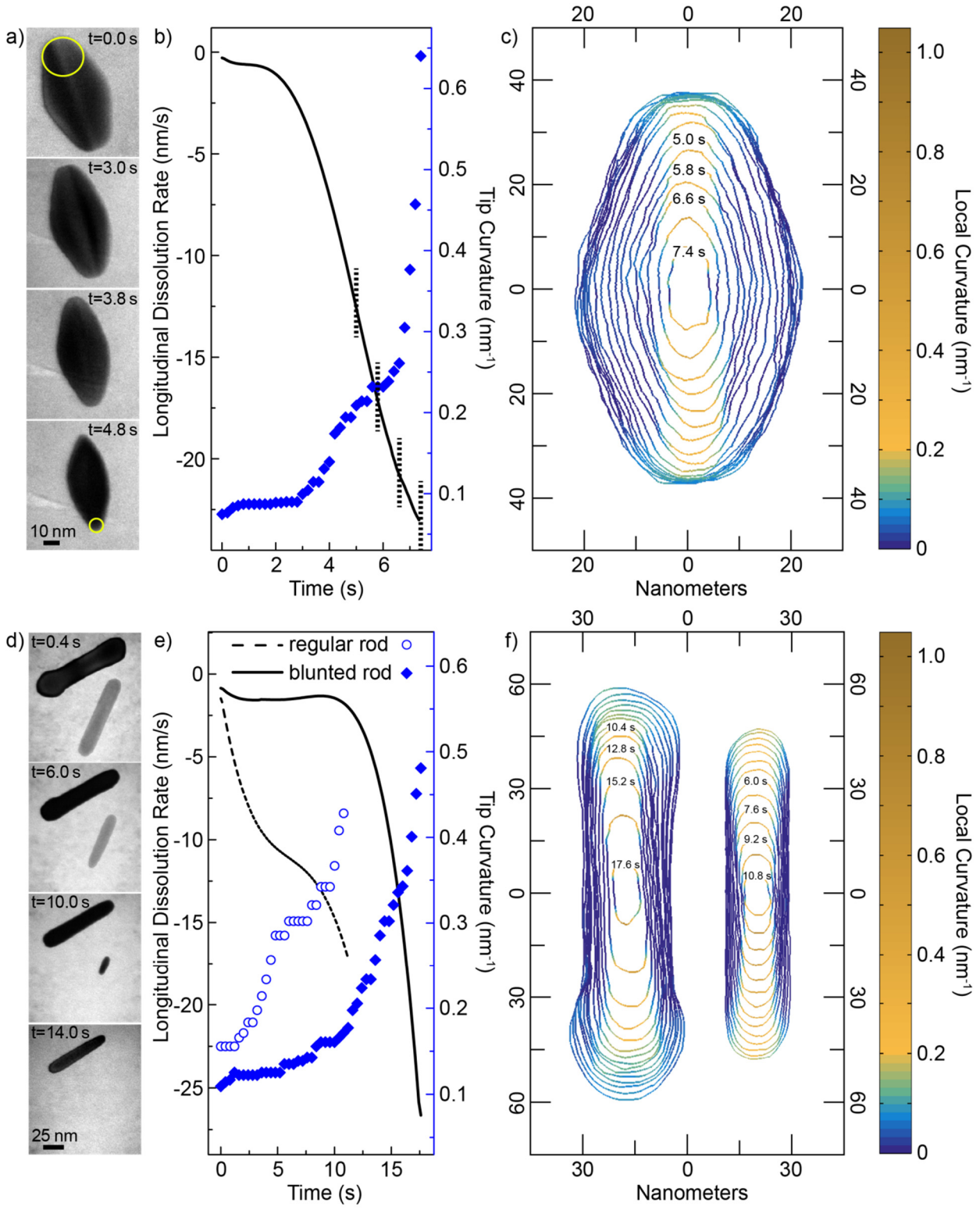

Figure S18. Characterization of additional oxidation reactions for pseudo-one-dimensional nanocrystals: pentagonal bipyramid (a-c) and a rod/blunted rod pair (d-f). Selected time-lapse TEM images extracted from Movies S15 (a) and S21 (d), plots of longitudinal dissolution rate and tip curvature as a function of time (b,e), and time-domain contour plots (c,f). Vertical dotted lines in (b, e) correspond to the time-labeled contours in (c, f). Contour lines are spaced in time by 0.4, 1.2, and 0.8 seconds for bipyramid (c), blunted rod (f) and rod (f), respectively.

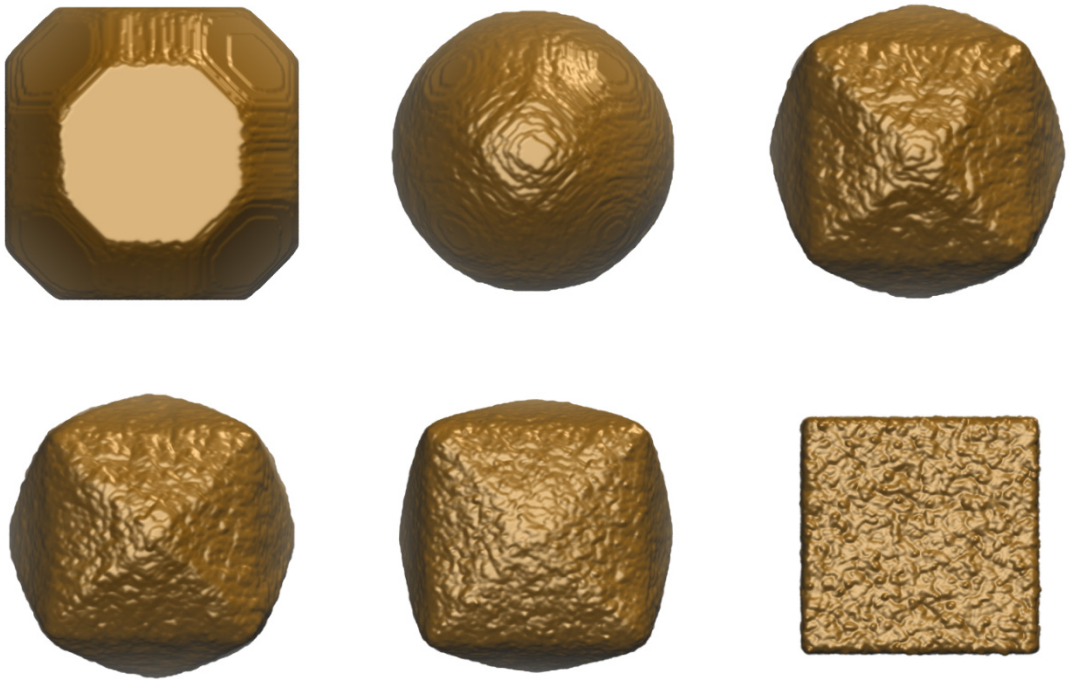

Figure S19. Initially cubic, ~7 million-atom nanoparticles etched, with both insertion and deletion moves allowed, at different values of the chemical potential: from left-to-right, top-to-bottom $\frac{\mu}{\epsilon}$ = -5.98, -6.0, -6.25, -6.75, -7.0, -8.0 (Movie S29). Low values of the chemical potential show equilibrium or near-equilibrium structures while higher values show the formation of the THH. Images are viewed down the ⟨100⟩ zone axis.

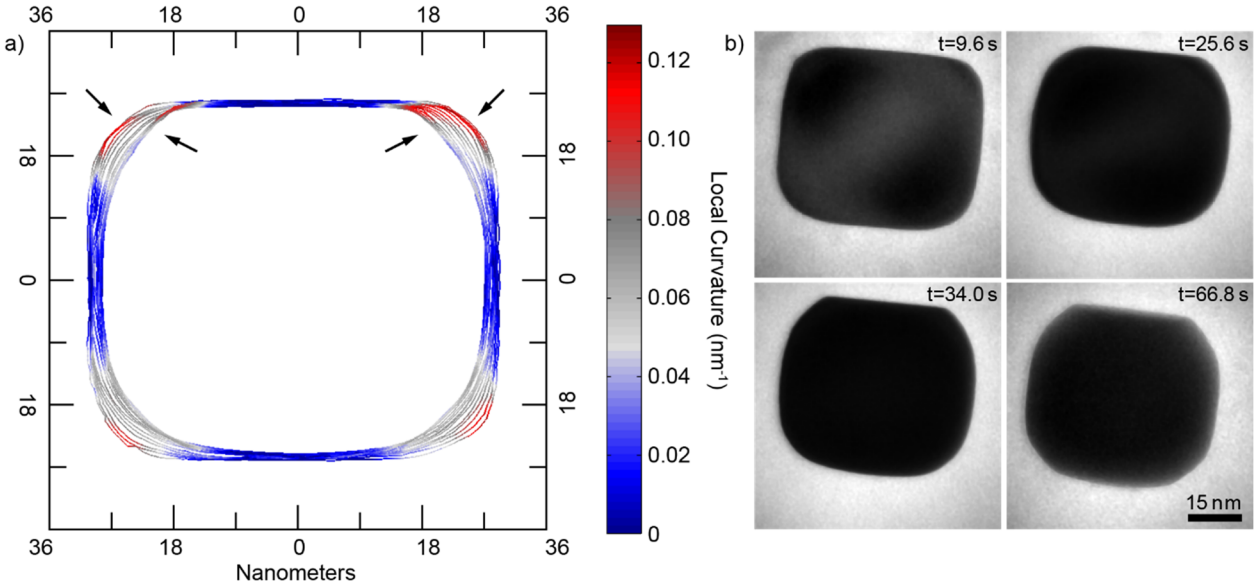

Figure S20. Time-domain contour plot (a) and selected time-lapse TEM images (b) for an equilibrium cube dissolution reaction conducted at reduced etchant concentration extracted from Movie S26. Note the initial appearance of sharp features (top set of arrows) which eventually develop into lower-energy blunt facets (bottom set of arrows, see Movie S27 for further illustration). Contour lines are spaced in time by 3.2 seconds. The electron dose rate was 86 electrons/$Å^2$·s.

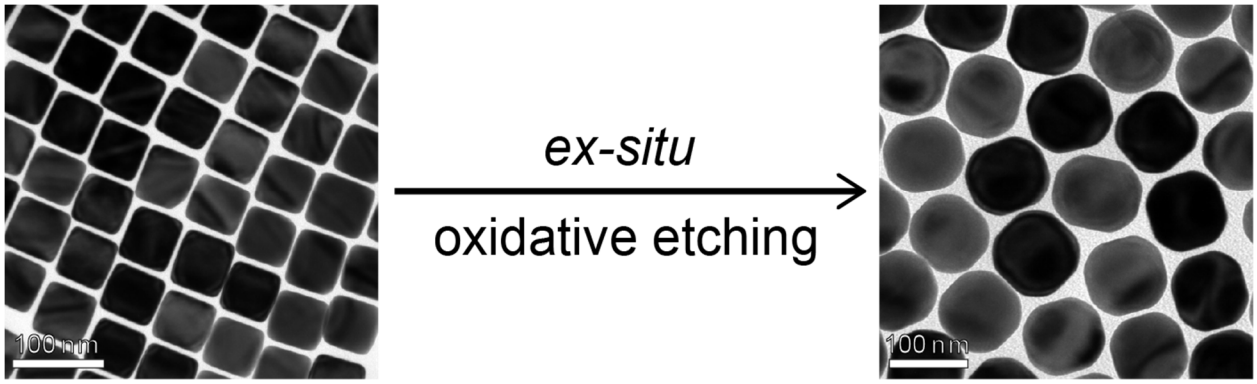

Figure S21. TEM images of ex-situ ensemble etching of gold cubes into truncated octahedra. Cubes were dissolved in 1.5 mL of 50 mM CTAB solution (OD = 3), to which 5 μL of 10 mM $HAuCl_4$ was added. The reaction was allowed to proceed for one hour at room temperature under 500 rpm stirring.

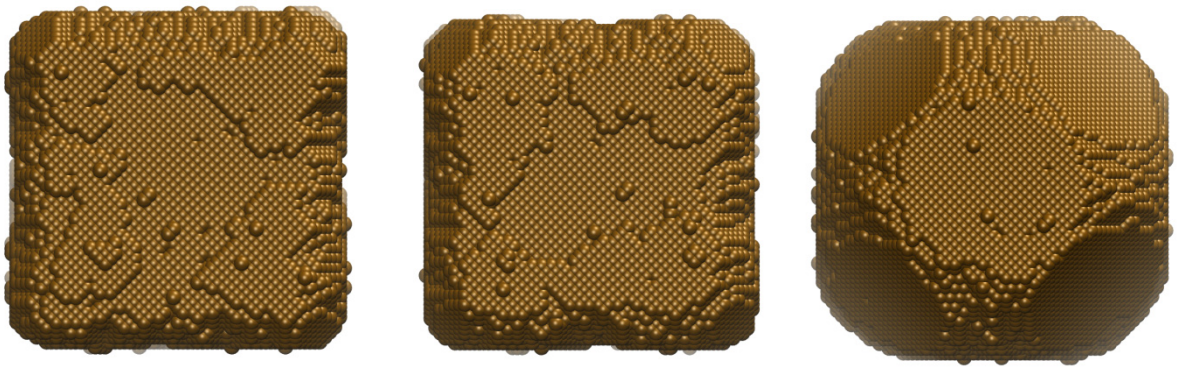

Figure S22. Surface diffusion of an initially cubic nanoparticle with ~130,00 atoms (Movie S28). From left to right: local diffusion, 2-local diffusion, global diffusion. Each case allows the system to relax to the equilibrium shape (truncated octahedron), albeit at different rates. Here, no etching (insertion or deletion moves) are allowed, and only diffusion moves occur.

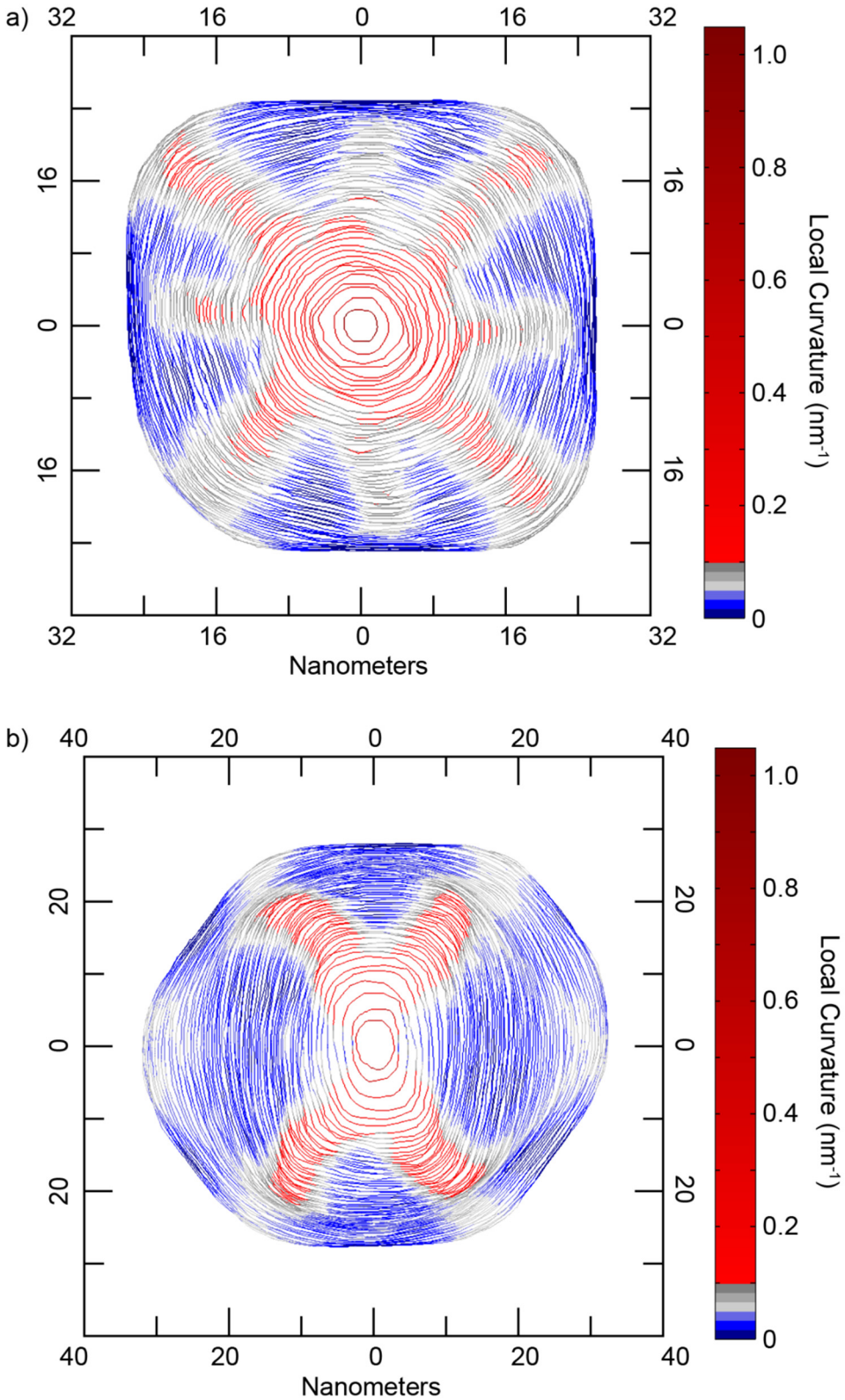

Figure S23. Complete dataset of time-domain contour plots for the cube (a) and rhombic dodecahedron (b) reactions shown in Figure 3. Contour lines are spaced in time by 0.4 seconds.

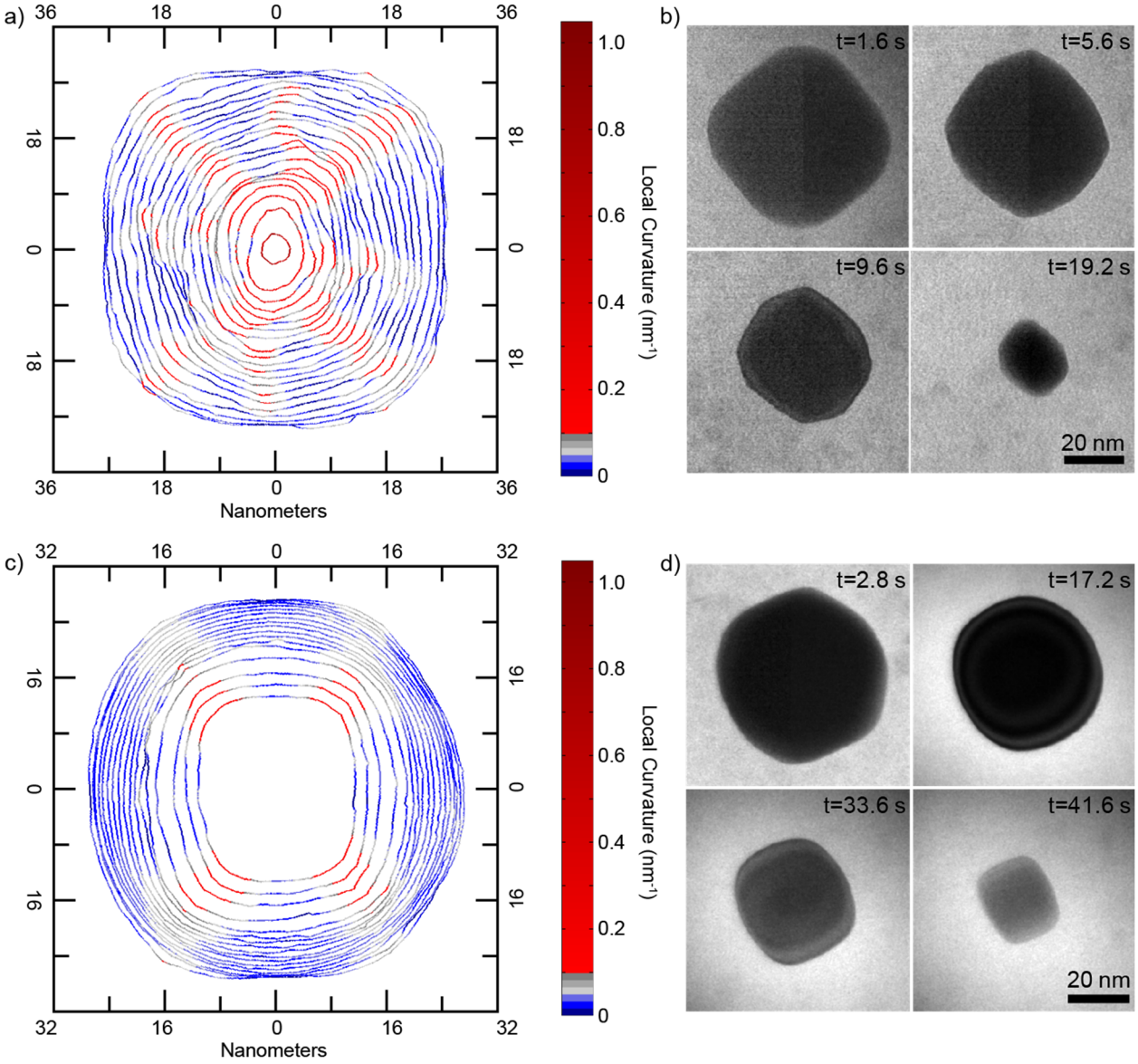

Figure S24. Time-domain contour plots and selected time-lapse TEM images of additional oxidative dissolution reactions for gold cube (a,b) and rhombic dodecahedron (c,d) nanocrystals extracted from Movies S23 and S33, respectively. Contour lines are spaced in time by 0.4 and 0.8 seconds in (a) and (c), respectively.

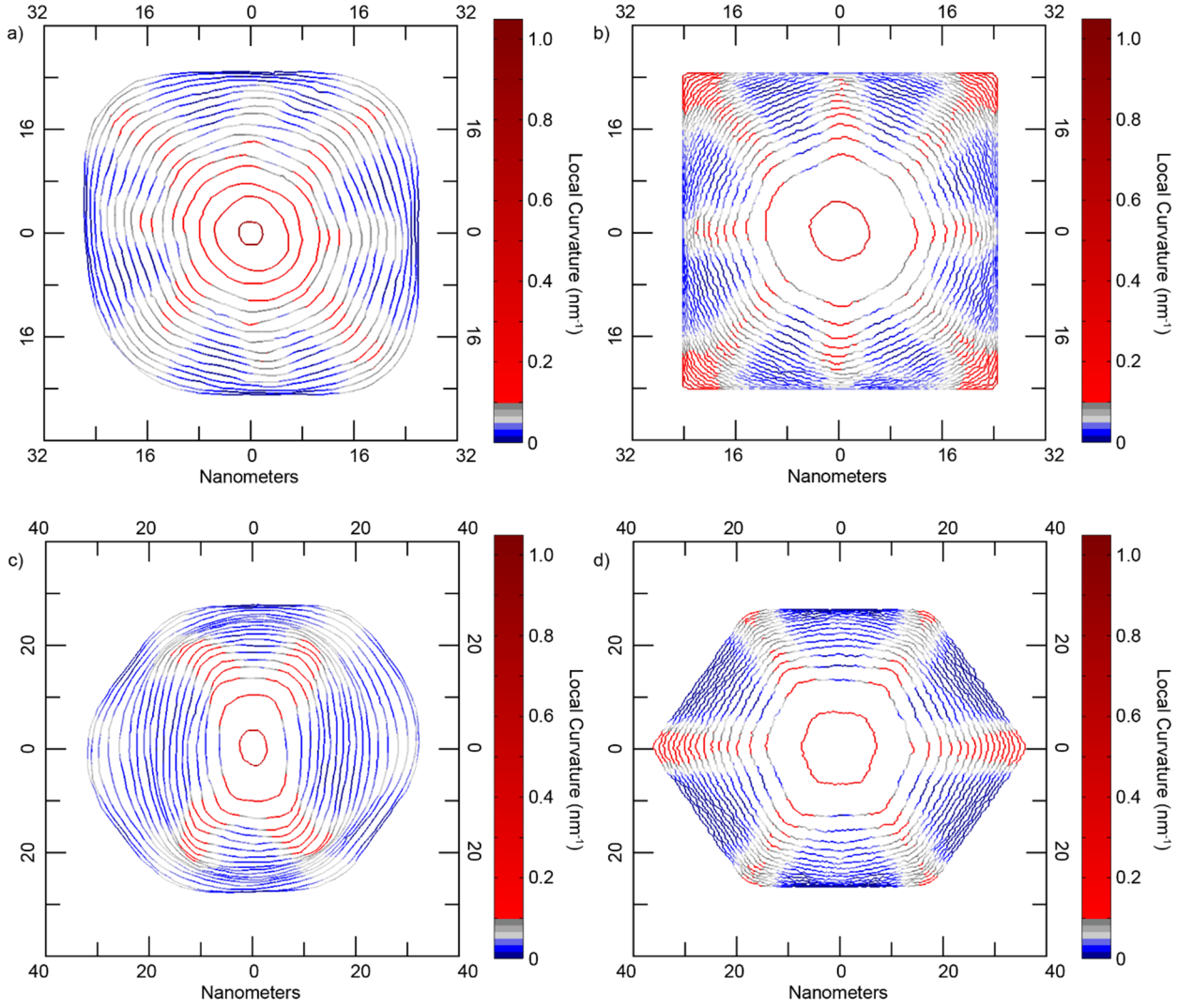

Figure S25. Comparison of contour plots extracted from experimental (a,c) and simulation (b,d) movies for cube (a,b) and rhombic dodecahedron (c,d) nanocrystal oxidation reactions extracted from Movies S22, S24, S32, and S34 for (a), (b), (c), and (d), respectively.

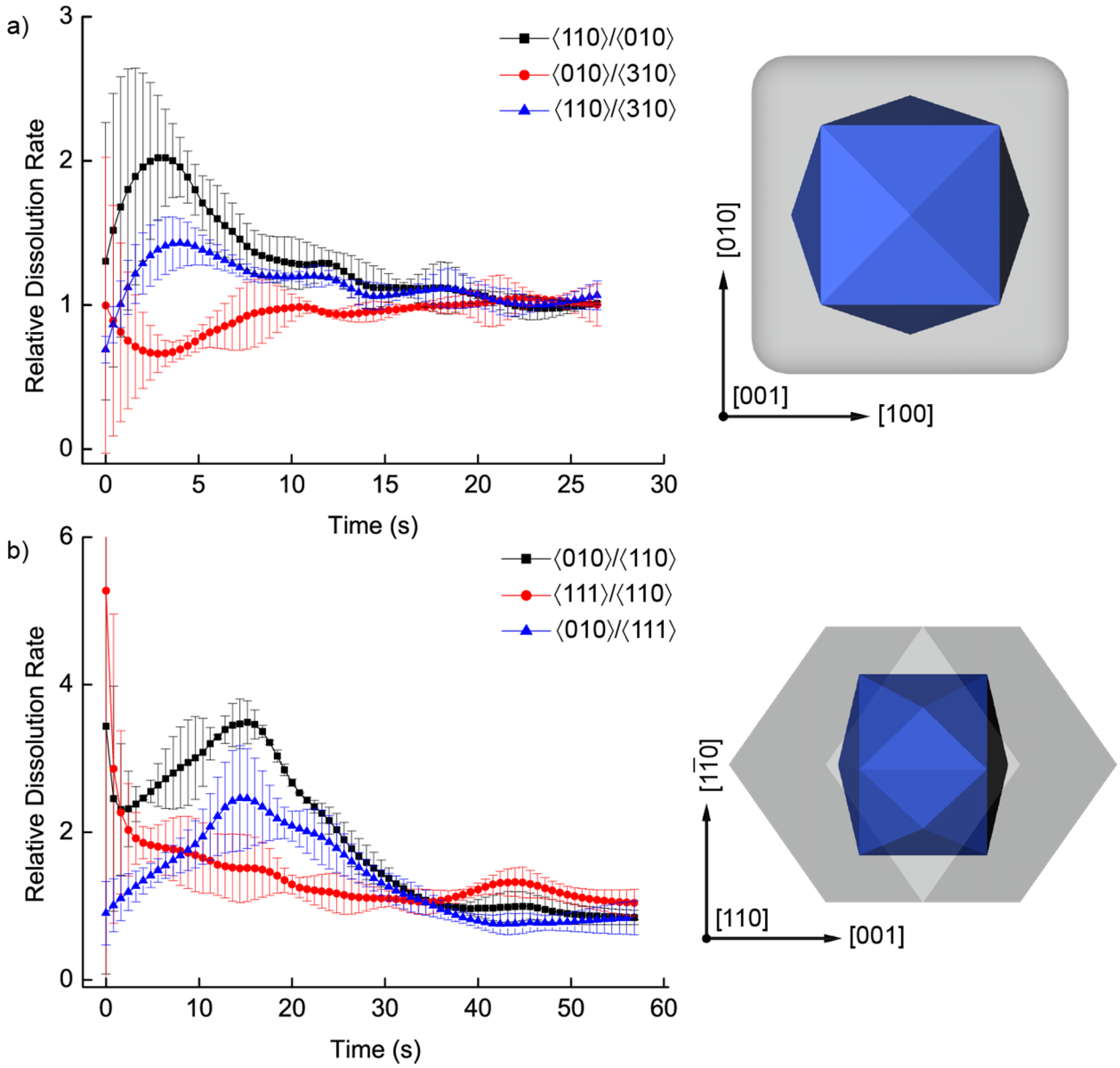

Figure S26. Ratio of crystallographic dissolution rates for cube (a) and rhombic dodecahedron (b) etching reactions presented in Figure 3. Schematic illustrations of the relevant crystallographic orientation are shown at right.

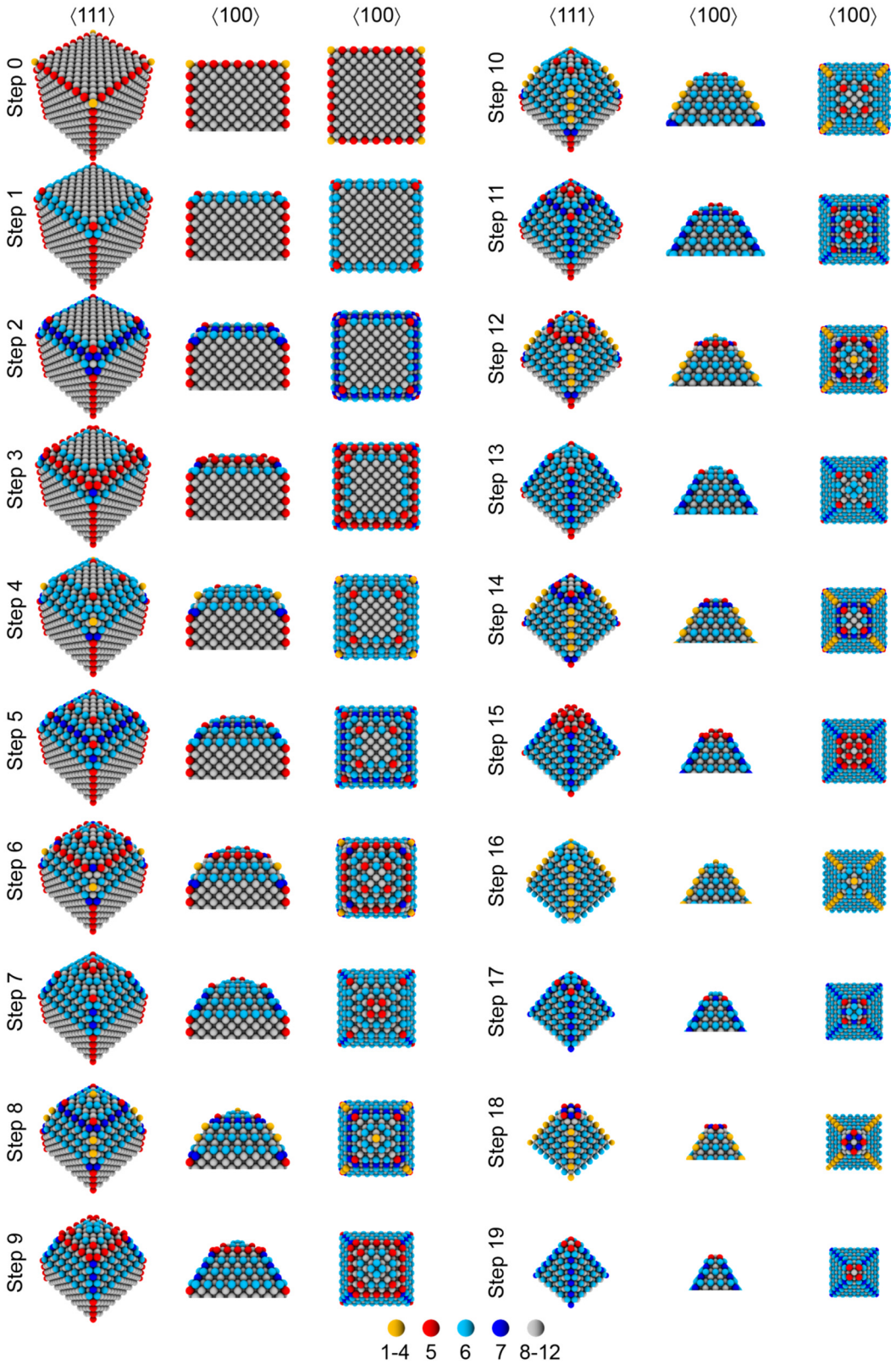

Figure S27. Idealized etching of a cube in which atoms with coordination number ≤ 6 are deterministically removed at each step. Several crystallographic perspectives are shown. Legend at bottom denotes the color value applied to atoms with different coordination numbers. Note the appearance and recession of {100} terraces via the removal of edge and corner atoms to create vicinal {210} facets. See also Movie S31.

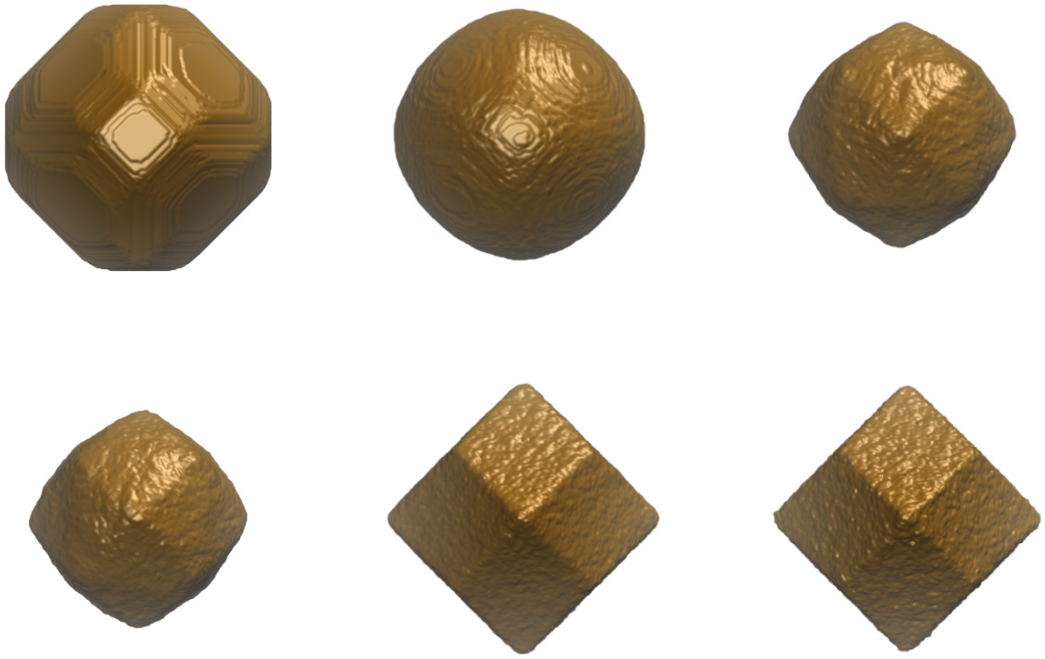

Figure S28. Initially rhombic-dodecahedral, ~6 million-atom nanoparticles etched, with both insertion and deletion moves allowed, at different values of the chemical potential: from left-to-right, top-to-bottom $\frac{\mu}{\epsilon}$ = -5.98, -6.0, -6.25, -6.75, -7.0, -8.0 (Movie S36). Images are viewed down the ⟨100⟩ zone axis.

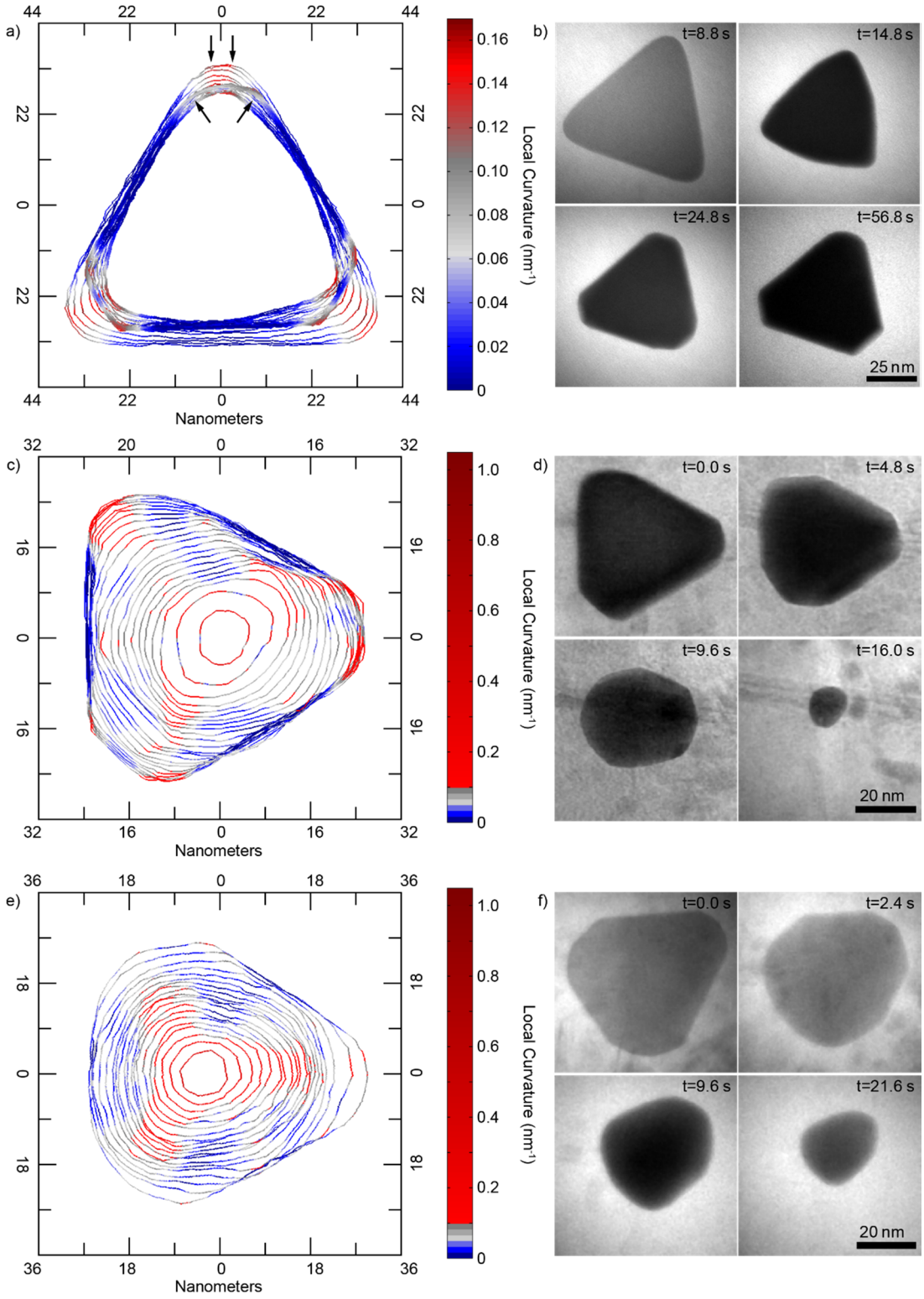

Figure S29. Time-domain contour plots and selected time-lapse TEM images of the oxidative dissolution of gold triangular prisms extracted from Movies S41 (a,b,), S43 (c,d) and S44 (e,f). At lower $FeCl_3$ concentrations, reactions are slow and the particle develops low-energy facets (a,b, see also Movie S42). At higher $FeCl_3$ concentrations, reactions are driven out of equilibrium and unusual intermediate shapes with 7 and 5 side facets are observed (c-f). Contour lines are spaced in time by 1.2 seconds in (a) and 0.8 seconds in (d) and (e). The electron dose rate was 217 and 86 electrons/$Å^2 \cdot s$ for (a,b) and (c-f), respectively.

S3. Supplementary Text

Discussion of nanoparticle products formed under equilibrium and non-equilibrium etching conditions. A perfect cubic nanocrystal consisting of an FCC material bound by {100} facets will have edges with coordination number (n) equal to 5 and corners with n = 3 (step 0, Fig. S27). In the equilibrium regime, atoms with n = 6 will fluctuate and atoms with n < 6 will etch. Therefore, the initial cube configuration will quickly experience etching of the tips and edges, revealing step edges with atoms that have n = 6 (step 1, Fig. S27). The surface of the nanoparticle then proceeds to relax, reorganizing so as to minimize the total free energy. As dictated by the Wulff construction,(*17*) the resulting surface-energy-minimizing shape is a truncated octahedron. This equilibrium shape transformation is observed in both experiment (Fig. S20, S22, Movies S26-S27) and simulation (Figs. S19, S21, Movies S28-S30). Capturing this shape change in simulations takes two forms. In the first, following the scheme outlined in the "Lattice gas Monte Carlo" section of S1, both insertion and deletion moves are allowed but the truncated octahedron is only observed within a narrow range of values of the chemical potential. In the second, diffusion-like MC moves that foster relaxation by transporting surface atoms to other sites on the nanoparticle surface, in a way that satisfies detailed balance, are introduced. However, the equilibrium shape is attained only when diffusion rates are much higher than those on an unperturbed nanocrystal. We thus propose that oxidative etching, in addition to removing material from a nanoparticle, renders its surface significantly more labile.

In the non-equilibrium case, the rate at which atoms with $n = 6$ are etched is made much greater than the rate at which atoms with $n = 7$ and higher are etched. In the language of the lattice gas model, the chemical potential is set such that deletion of surface atoms with n = 6 is facile, whereas insertion of such atoms is not. As a result, after the initial edge (n = 5) and tip (n =3) atoms are removed and the step edges (n = 6) are revealed (step 1, Fig. S27), the system continues to experience etching rather than being allowed to equilibrate to the minimum-energy Wulff shape. As the first n = 6 edges withdraw, new step edges are revealed which also have n = 6. This results in persistent recession of {100} terraces whose periphery are always defined by n = 6 atoms. Eventually, a step train is formed: a vicinal surface with equidistant steps (steps 7-19, Fig. S27).(*18*) This process is the etching equivalent of the well-known step-flow crystal growth

mechanism first described by Burton, Cabrera, and Frank in 1951.(*19*) In the main text, we have referred to it as "step recession". Since step recession occurs with equal velocity from all four sides of the initial {100} facets, receding edges will eventually meet in the center of the original cube face. The resulting feature that remains will be a square pyramid whose angle with respect to the {100} plane will be defined by the ratio of step height to terrace width in the step train. This is equivalent to describing the facets as vicinal {hk0} where h>k and the ratio h/k is related to the angle of the pyramidal feature. The shape that results when these pyramidal features form on each of the six faces of the original cube is a tetrahexahedron (THH, Movie S31). Because the chemical potential will continually generate edges with $n = 6$ via step recession, a non-equilibrium steady-state condition is achieved in which the THH shape is transiently stable so long as the rate of etching is considerably faster than the rate at which the system can relax (see below).

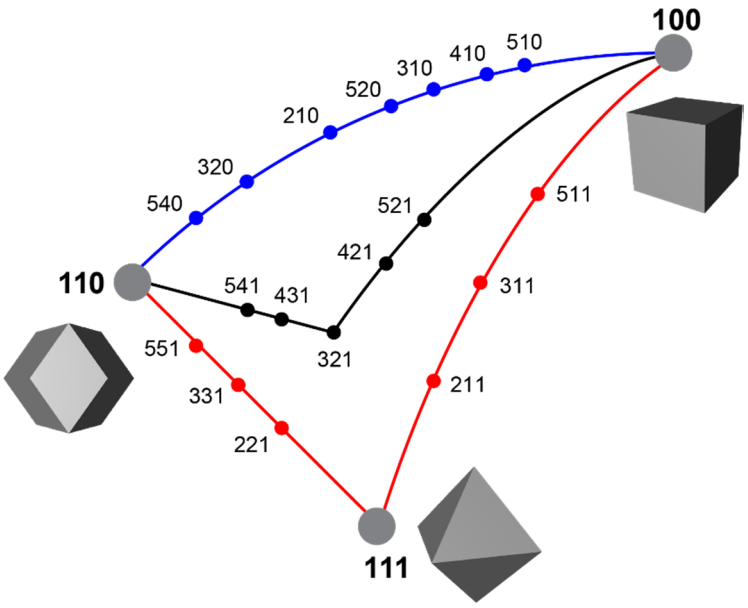

Figure S30. Stereographic triangle connecting the low-index poles of an FCC metal with their nanocrystal representations of cube {100}, rhombic dodecahedron {110}, and octahedron {111} particles. Cube and rhombic dodecahedron particles are connected by a series of {hk0}-bound particles, all of which represent tetrahexahedra with different pyramidal angles (θ, see Fig. 4b, inset).

The stereographic projection is a useful tool for illustrating the connection between different crystallographic surface facets by representing all {hkl} planes as points (also called poles) on a two-dimensional surface that preserves the angular relationship between them. Paths connecting two points represent possible transitions between planes that proceed through numerous gradual changes in miller indices and surface energy. If instead of viewing these pathways as transitions

between atomic planes they are imagined as transitions between nanocrystals bound in these {hkl} surface facets, potential shape transformation reactions can be generated.(*20-22*) When applied to a system with cubic symmetry, it can be seen that {100}-bound cube and {110}-bound rhombic dodecahedron nanocrystals can both transform into particles bound by {hk0} facets through relatively small movements in stereographic space (i.e., small changes in the crystallographic angles of their faces, Fig. S30). As mentioned above, any {hk0}-bound single crystalline shape (where h>k≥1) will be a tetrahexahedron where the angle of the pyramidal feature with respect to the {100} facet (θ) is defined by:

$$\theta = \cos^{-1}\left(\frac{h}{\sqrt{h^2 + k^2}}\right)$$

Therefore, although the cube and rhombic dodecahedron nanocrystal both transition to {210} THH intermediates in simulations, they do so from opposite poles in the stereographic projection and, as a result, necessarily follow distinct pathways (Fig. S30). While the cube will approach the {210} THH (θ = 26.6) by transitioning through several other THH particles defined by {h10} vicinal facets (θ < 26.6), the rhombic dodecahedron (θ = 45) will instead access the {210} through THH particles defined by non-vicinal facets (θ >26.6). This explains the observation in simulations of a {310} THH as one of the intermediate products of the cube etching reaction but not in the rhombic dodecahedron etching reaction.

Interestingly, for both the cube and the rhombic dodecahedron etching reactions, simulations predict the steady-state kinetic product to be a {210} THH while the measured experimental structure is a {310} THH (Fig. 3, 4). As mentioned in the main text, this discrepancy likely arises from factors which are not accounted for in the simulations. One intriguing possibility involves the role of the CTAB ligands in directing the stability of different vicinal surfaces. Several groups have reported evidence of selective binding of CTAB to {100} compared to other low-index facets in FCC metal nanocrystals.(*23-25*) Since the {310} facet has a larger {100} terrace area compared to the {210} (Fig. 4c, d), CTAB ligands may be able to more effectively bind and stabilize these facets. Therefore, although the appearance of {310} THH intermediates is mostly driven by non-equilibrium coordination number-based processes (see above), a competing effect

that favors more open vicinal facets may be driven by ligand binding. The nuances of these ligand effects will be the subject of future investigations.

Effect of varying parameters. To test the robustness of our Monte Carlo model, we investigated the behavior of the system for different particle sizes and different values of the chemical potential. Simulations conducted with three different nanoparticle sizes (1 million, 7 million, and 55 million atoms) etching at $\mu/\varepsilon = -6.5$ are shown below (Figs. S31-S32). In each case, it is clear that regardless of the size, the limiting shape under non-equilibrium conditions is a THH.

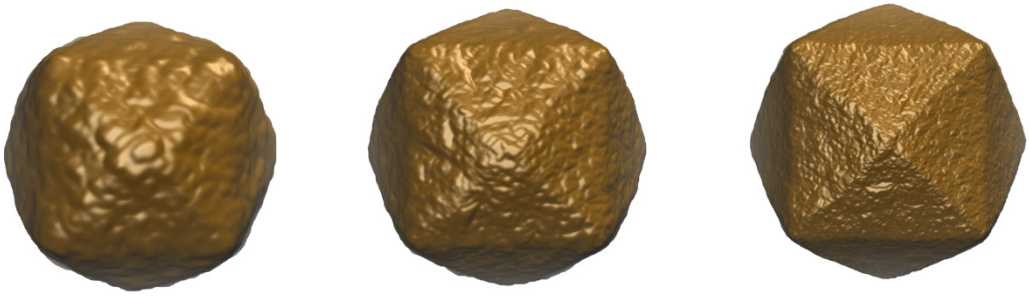

Figure S31. Left to right: nanoparticles which were initially cubic, with sizes of ~1, 7, and 55 million atoms, all etched to THH configurations at $\frac{\mu}{\epsilon} = -6.5$ (Movie S45). Images are viewed down the ⟨100⟩ zone axis.

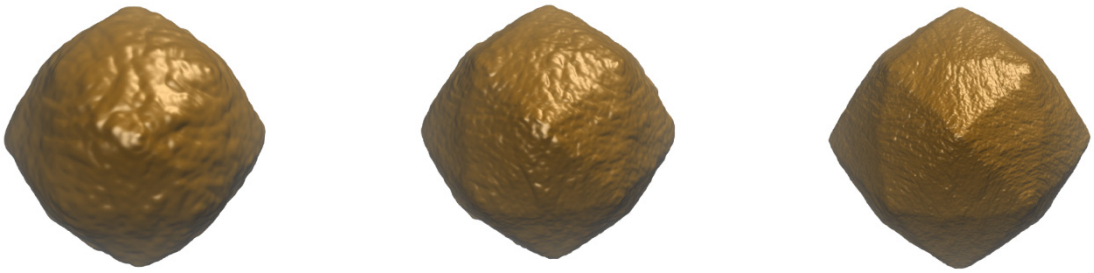

Figure S32. Left to right: nanoparticles which were initially rhombic dodecahedra, with sizes of ~1, 6, and 50 million atoms, all etched to THH configurations at $\frac{\mu}{\epsilon} = -6.5$ (Movies S46-S47). Images are viewed down the ⟨100⟩ zone axis.

To probe the effect of chemical potential on non-equilibrium shape transformation, simulations were conducted at a number of different values of μ/ε (Figs. S19, S28, and Movies S29-S30, S36-S39). It appears that since the THH intermediate is generated over a range of different values of the chemical potential, the THH is a rather general non-equilibrium steady-state configuration for etching of an FCC lattice.

It was observed experimentally that for very high dose rates (effective driving force), the intermediate structure stays cubic or nearly cubic for the entire reaction (Fig. S33, Movie S48). This is precisely what is observed upon increasing the chemical potential to $\mu/\epsilon = -8$ in the Glauber dynamics simulations (Fig. S19, Movie S29).

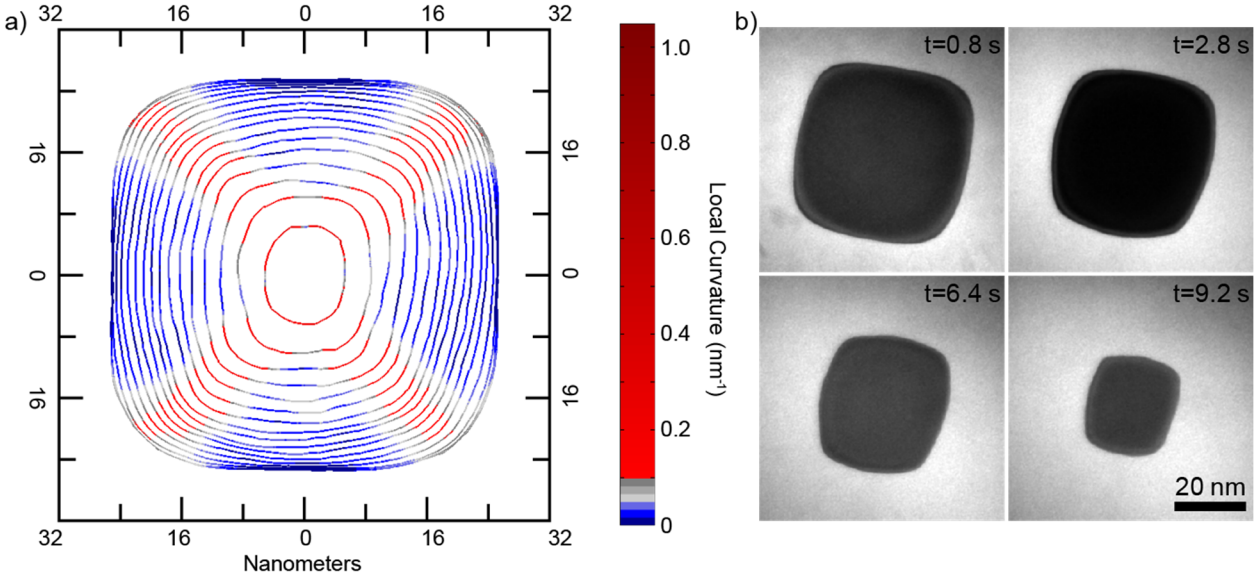

Figure S33. Time-domain contour plot and selected time-lapse TEM images of a cube etching reaction extracted from Movie S48. The higher driving force (electron dose rate of 217 electrons/Å^2·s) suppresses the observation of the THH intermediate, as predicted by simulations (see Fig. S19 and Movie S29). Contour lines are spaced in time by 0.8 seconds.

We also note that we can induce nanoparticle *growth* by increasing the chemical potential to values significantly greater than $\frac{\mu}{\epsilon} = -6.0$ (Fig. S34).

Figure S34. Growth of an initially cubic nanoparticle of size ~7 million atoms via nucleation on the {100} surfaces for the case of $\frac{\mu}{\epsilon} = -5.0$ (Movie S29).

Note that when the system is precisely at coexistence ($\frac{\mu}{\epsilon} = -6.0$) the nanoparticle etches to a seemingly featureless, spherical shape, and continues etching, gradually, until it disappears completely (Movies S29-S30, S36-S39). As discussed in S1, though, the instability of finite (non-macroscopic) phases at coexistence is actually predicted by classical nucleation theory.(*13*) Therefore, to observe the equilibrium structure, we must use a chemical potential slightly above coexistence – hence our choice of $\frac{\mu}{\epsilon} = -5.98$ for the equilibrium etching simulation.

Effect of diffusion.

As discussed in section S1, we expect that some type of etchant-mediated diffusion, rather than the insertion moves of the lattice gas model, is a plausible mechanism for nanoparticle surface relaxation. To obtain a better sense of the nature of this diffusion process, we subjected simulated nanoparticles to several types of diffusion, described in section S1. Snapshots of an initial cubic nanocrystal containing ~130,000 atoms subjected to these different types of diffusion, with no etching moves allowed are shown in Fig. S22. Here, we chose $\epsilon_{diff} = \epsilon/5$, to make the barrier to diffusion lower than the energetic barrier to etching (presumably diffusion is a less violent bond-breaking process than etching) and hence the diffusion rate higher. All the simulations show that the nanoparticles are heading towards a truncated octahedron shape - the corners disappear and form {111} facets while the side {100} faces shrink in area but grow additional layers. However, for the same number of attempted diffusion moves (1×10^9), global diffusion approximates the equilibrium truncated octahedron shape much more closely than

either local or 2-local diffusion. It is apparently much easier, and takes fewer MC steps, to attain the equilibrium shape using global diffusion than using either local or 2-local diffusion.

We also performed simulations where both etching and surface diffusion moves were allowed. Here, we examined ~7 million-atom nanoparticles, with the chemical potential set to $\mu/\epsilon = -6.5$. We attempted global diffusion moves with a probability R for values $R = 0.9, 0.99, 0.999$. (For values much less than 0.9, the presence of diffusion moves had essentially no effect on the shape evolution.) Deletion moves and insertion moves were both attempted with probability $(1 - R)/2$ though insertion moves were accepted at a rate so small as to be negligible (Fig. S35). As can be seen, for sufficiently large R, surface diffusion dominates etching, resulting in the attainment of the equilibrium, truncated octahedron shape.

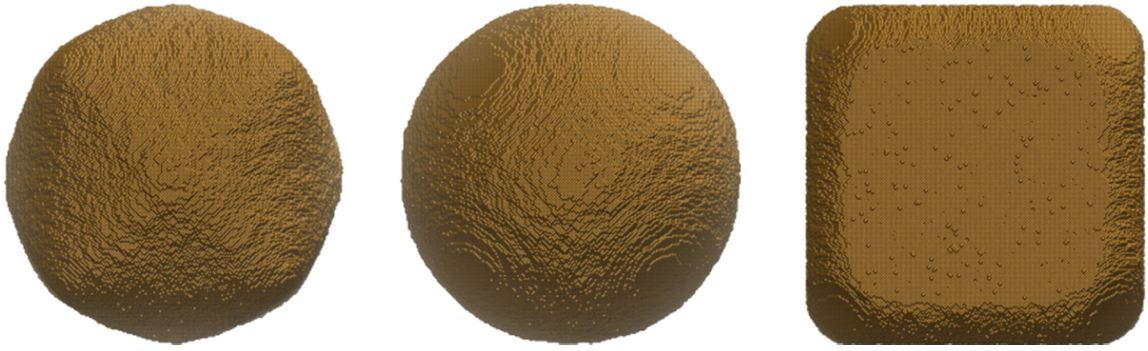

Figure S35. Left to right: ~7-million-atom nanoparticles which were initially cubic, subjected to a combination of global diffusion and etching moves, with diffusion *attempt* probabilities R =0.9, 0.99, and 0.999. The ratios of *accepted* diffusion moves to etching moves were ≈2, 21, and 260, respectively. Etching was done at $\frac{\mu}{\epsilon} = -6.5$. Images are viewed along the ⟨100⟩ zone axis.

Effect of Monte Carlo Dynamics. A number of different Monte Carlo algorithms have been used to simulate nanocrystal systems. Here we compare Glauber dynamics (implemented for the majority of the data presented here) to Metropolis dynamics (*26*) and to the kinetic Glauber scheme described in S1. Metropolis dynamics is implemented in a way nearly identical to Glauber dynamics; for Metropolis dynamics, though, the acceptance probabilities are given by:

$$A_{insert}(C \to C') = \min\left[1, \frac{N_{vac}(C)}{N_{surf}(C')} e^{-\beta \Delta H}\right],$$

$$A_{delete}(C \to C') = \min\left[1, \frac{N_{surf}(C)}{N_{vac}(C')} e^{-\beta \Delta H}\right],$$

$$\Delta H = H(C') - H(C).$$

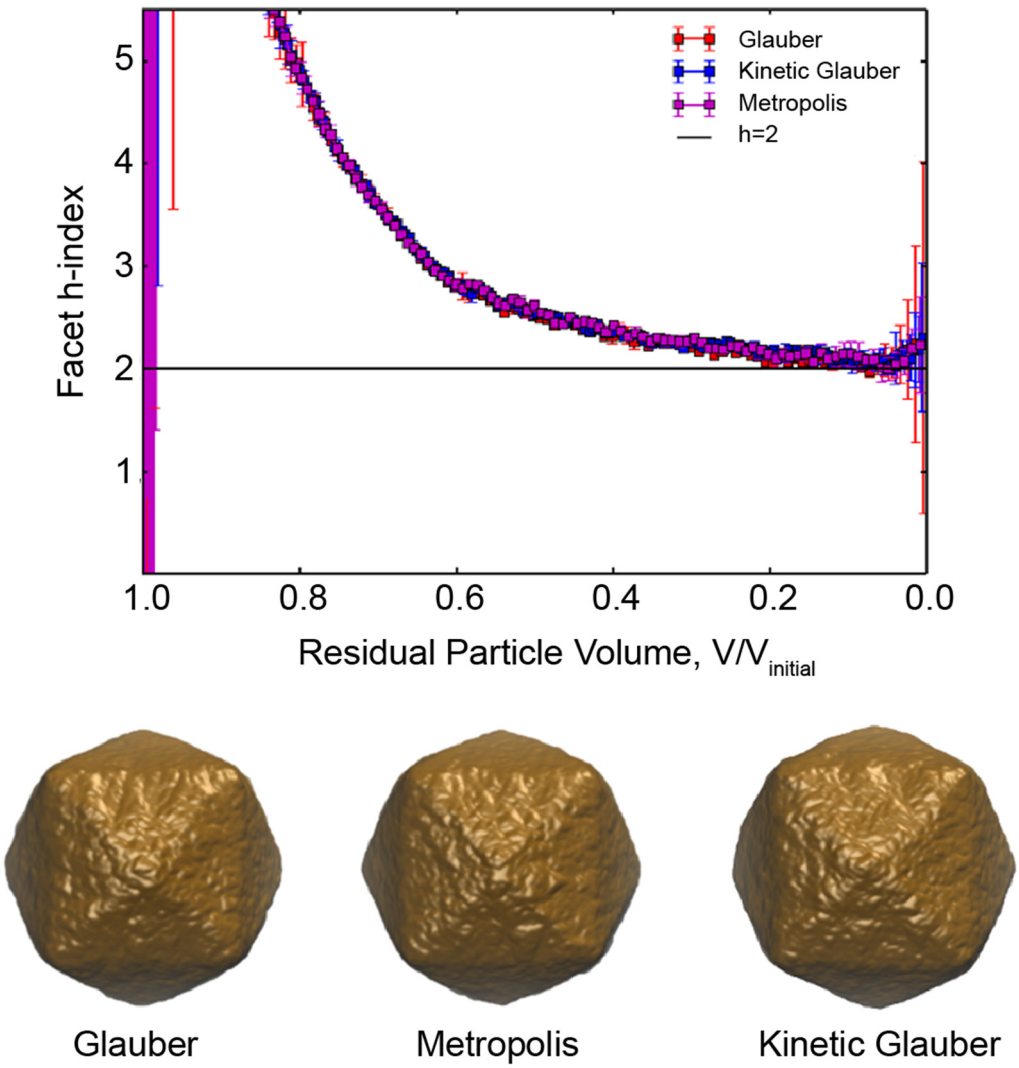

Figure S36. Comparison of etching structures generated with three different types of dynamics (Glauber, Metropolis, and kinetic Glauber).) Each nanoparticle image represents a configuration where $V/V_{init} \approx 0.3$. For the Metropolis dynamics, the number of attempted steps was ~1.34×10^8 and the acceptance ratio was ~0.0526 and for the Glauber dynamics the number of attempted steps was ~1.34×10^8 and the acceptance ratio was ~0.0524.

When the chemical potential is set to $\mu/\epsilon = -6.5$ (for the Glauber and Metropolis dynamics), the etching structures that result from the three types of algorithms appear nearly identical and are indeed THH shapes; quantification of the h-index over time shows that they are statistically indistinguishable (Fig. S36). The appearance of a THH during etching thus appears to be robust to the specific choice of dynamics.

S4. List of Supplementary Movies

Movie S1. TEM movie of partial dissolution of a gold nanorod followed by tip re-faceting and development of {100} planes. The concentration of $FeCl_3$ was 0.02 M in the GLC loading solution. The acquisition frame rate is 2.5 fps. Two movies were recorded back-to-back with a dead time of 6 seconds between them, and were concatenated into a single movie. The electron dose rate was 217 electrons/$Å^2$·s.

Movie S2. TEM movie of dissolution of a regular gold nanorod (89.1 nm x 27.4 nm). The acquisition frame rate is 5.0 fps. The electron dose rate was 217 electrons/$Å^2$·s. The concentration of $FeCl_3$ was 0.03 M in the GLC loading solution.

Movie S3. TEM movie of a gold nanorod dispersed in Tris buffer (pH=8.2). No etching was observed under prolonged electron-beam illumination (~60 seconds). The acquisition frame rate is 2.5 fps. The electron dose rate was 217 electrons/$Å^2$·s.

Movie S4. TEM movie of a gold nanorod dispersed in an acidified Tris buffer solution (pH=0.92) without $FeCl_3$. No etching was observed under prolonged electron-beam illumination (~60 seconds). The acquisition frame rate is 2.5 fps. The electron dose rate was 217 electrons/$Å^2$·s.

Movie S5. TEM movie of a Au@SiO_2 core-shell nanorod dispersed in a mixture of Tris buffer and acidified $FeCl_3$ solutions (final [$FeCl_3$] =0.04 M, pH=0.92). No etching was observed under prolonged electron-beam illumination (~90 seconds). The acquisition frame rate is 2.5 fps. The electron dose rate was 217 electrons/$Å^2$·s.

Movie S6. TEM movie of gold nanorods dispersed in a mixture of Tris buffer, acidified $FeCl_3$ and isopropanol (final [$FeCl_3$] =0.04 M, [isopropanol] =0.15M, pH=0.92). No etching was observed under prolonged electron-beam illumination (~45 seconds). The acquisition frame rate is 2.5 fps. The electron dose rate was 86 electrons/$Å^2$·s.

Movie S7. TEM movie of a gold nanorod dispersed in a mixture of Tris buffer, acidified $FeCl_3$ and isopropanol (final [$FeCl_3$] =0.04 M, [isopropanol] =0.15M, pH=0.92). No etching was observed under prolonged electron-beam illumination (~55 seconds). The acquisition frame rate is 2.5 fps. The electron dose rate was 254 electrons/$Å^2$·s.

Movie S8. TEM movie of a gold nanorod dispersed in a mixture of Tris buffer, acidified $FeCl_3$ and isopropanol (final [$FeCl_3$] =0.02 M, pH=0.92). A negligible degree of etching was observed after prolonged electron-beam illumination (~60 seconds). The acquisition frame rate is 2.5 fps. The electron dose rate was 217 electrons/$Å^2$·s.

Movie S9. High-resolution TEM movie of partial dissolution of a gold nanorod followed by tip re-faceting and development of {100} planes. The concentration of $FeCl_3$ was 0.02 M in the GLC loading solution. The acquisition frame rate is 400 fps. The original full field of view was binned by 4 before movie extraction. The electron dose rate was about 1500 electrons/$Å^2$·s. This movie was acquired with the 300 kV aberration-corrected TEAM I microscope at the National Center for Electron Microscopy facility within The Molecular Foundry at Lawrence Berkeley National Laboratory.

Movie S10. TEM movie of dissolution of a regular gold nanorod (84.3 nm x 23.2 nm). The acquisition frame rate is 2.5 fps. The electron dose rate was 217 electrons/$Å^2$·s.

Movie S11. Monte Carlo simulation movie of a 2-million-atom nanorod etched at the chemical potential $\frac{\mu}{\epsilon}$ = -5.98 and -6.5. For the near-equilibrium rod etching at $\frac{\mu}{\epsilon}$ = -5.98, the number of attempted steps was 5.00×10^7 and the acceptance ratio was ~0.0317. For the non-equilibrium rod etching at $\frac{\mu}{\epsilon}$ = -6.5, the number of attempted steps was ~3.00×10^7 and the acceptance ratios was ~0.0677. Images are viewed along the ⟨100⟩ zone axis.

Movie S12. Contour plot movie showing the progression of nanocrystal local curvature for the equilibrium rod dissolution reaction shown in Figure 1 and Movie S1. Five contours are shown at any given time to better illustrate the development of low-energy blunt facets.

Movie S13. TEM movie of dissolution of a blunted gold nanorod. The acquisition frame rate is 2.5 fps. The electron dose rate was 217 electrons/$Å^2$·s.

Movie S14. TEM movie of dissolution of an additional blunted gold nanorod. The acquisition frame rate is 2.5 fps. The electron dose rate was 217 electrons/$Å^2$·s. The concentration of $FeCl_3$ was 0.03 M in the GLC loading solution.

Movie S15. TEM movie of dissolution of a gold pentagonal bipyramid. The acquisition frame rate is 5.0 fps. The electron dose rate was 217 electrons/$Å^2$·s.

Movie S16. TEM movie of partial dissolution of a gold decahedron that exhibits tip-selective blunting. The acquisition frame rate is 2.5 fps. The electron dose rate was 86 electrons/$Å^2$·s. The concentration of $FeCl_3$ was 0.03 M in the GLC loading solution.

Movie S17. TEM movie of partial dissolution of a gold rhombic dodecahedron that exhibits tip-selective blunting. The acquisition frame rate is 2.5 fps. The electron dose rate was 86 electrons/$Å^2$·s. The concentration of $FeCl_3$ was 0.03 M in the GLC loading solution.

Movie S18. TEM movie of dissolution of a gold triangular bipyramid, found as an impurity shape in the gold octahedron synthesis, that exhibits tip-selective blunting. The acquisition frame rate is 5.0 fps. The electron dose rate was 86 electrons/$Å^2$·s.

Movie S19. TEM movie of partial dissolution of a gold octahedron that exhibits tip-selective blunting. The acquisition frame rate is 2.5 fps. The electron dose rate was 86 electrons/$Å^2$·s. The concentration of $FeCl_3$ was 0.03 M in the GLC loading solution.

Movie S20. TEM movie of dissolution of a gold triangular prism. The acquisition frame rate is 2.5 fps. The electron dose rate was 217 electrons/$Å^2$·s.

Movie S21. TEM movie of simultaneous dissolution of a regular and blunted gold nanorod. The acquisition frame rate is 2.5 fps. The electron dose rate was 217 electrons/$Å^2$·s.

Movie S22. TEM movie of dissolution of a gold cube exhibiting the tetrahexahedron transient intermediate shape. The acquisition frame rate is 2.5 fps. The electron dose rate was 86 electrons/$Å^2$·s.

Movie S23. TEM movie of dissolution of an additional gold cube exhibiting the tetrahexahedron transient intermediate shape. The acquisition frame rate is 2.5 fps. The electron dose rate was 86 electrons/$Å^2$·s.

Movie S24. Monte Carlo simulation movie of a cubic, 7-million-atom nanocrystal etched at the chemical potential $\frac{\mu}{\epsilon}$ = -6.5. The number of attempted Monte Carlo steps was ~1.34×10^8, and the acceptance ratio was ~0.0524. The nanocrystal is viewed along the ⟨100⟩ zone axis.

Movie S25. Monte Carlo simulation movie of a cubic, 7-million-atom nanocrystal etched at the chemical potential $\frac{\mu}{\epsilon}$ = -6.5. The number of attempted Monte Carlo steps was ~1.34×10^8, and the acceptance ratio was ~0.0524. The nanocrystal is viewed along the ⟨100⟩ zone axis and the atoms are color-coded according to their coordination numbers.

Movie S26. TEM movie of equilibrium etching of a gold cube. The acquisition frame rate is 2.5 fps. The electron dose rate was 86 electrons/Å^2·s. The concentration of $FeCl_3$ was 0.02 M in the GLC loading solution.

Movie S27. Contour plot movie showing the progression of nanocrystal local curvature for the equilibrium cube dissolution reaction shown in Movie S27. Five contours are shown at any given time to better illustrate the development of low-energy blunt facets.

Movie S28. Monte Carlo simulation movie of atomic surface diffusion of a cubic, 1.3-million-atom nanocrystal. The number of attempted moves for local, 2-local, and global was 2×10^9, and the acceptance ratios were ~6.82×10^{-3}, 2.71×10^{-3}, and 6.50×10^{-3}, respectively. For "2-local long", 2×10^{10} steps were attempted instead. The nanocrystal is viewed along the ⟨100⟩ zone axis.

Movie S29. Monte Carlo simulation movies of a cubic, 7-million-atom nanocrystal etched at different values of the chemical potential: from left-to-right, top-to-bottom $\frac{\mu}{\epsilon}$ = -5.0, -5.98, -6.0, -6.25, -6.5, -6.75, -7.0, -8.0. The numbers of attempted Monte Carlo steps were: ~1×10^9, 2×10^{10}, 2.49×10^9, 1.44×10^8, 1.34×10^8, 1.29×10^8, 8.14×10^7, 3.84×10^7, respectively, and the corresponding acceptance ratios were: ~1.18×10^{-2}, 1.32×10^{-2}, 3.51×10^{-2}, 5.26×10^{-2}, 5.24×10^{-2}, 5.68×10^{-2}, 9.86×10^{-2}, 0.189. The nanocrystals are viewed along the ⟨100⟩ zone axis.

Movie S30. Monte Carlo simulation movies of a cubic, 7-million-atom nanocrystal etched at different values of the chemical potential: from left-to-right, top-to-bottom $\frac{\mu}{\epsilon}$ = -5.0, -5.98, -6.0, -6.25, -6.5, -6.75, -7.0, -8.0. The numbers of attempted Monte Carlo steps were: ~1×10^9, 2×10^{10}, 2.49×10^9, 1.44×10^8, 1.34×10^8, 1.29×10^8, 8.14×10^7, 3.84×10^7, respectively, and the corresponding acceptance ratios were: ~1.18×10^{-2}, 1.32×10^{-2}, 3.51×10^{-2}, 5.26×10^{-2}, 5.24×10^{-2}, 5.68×10^{-2}, 9.86×10^{-2}, 0.189. The nanocrystals are viewed along the ⟨100⟩ zone axis and the atoms are color-coded according to their coordination numbers.

Movie S31. Movie of the idealized etching of a cubic nanocrystal where atoms with coordination number ≤ 6 are deterministically removed at each step.

Movie S32. TEM movie of dissolution of a gold rhombic dodecahedron exhibiting the tetrahexahedron transient intermediate and final cube shapes. The acquisition frame rate is 2.5 fps. The electron dose rate was 86 electrons/Å^2·s.

Movie S33. TEM movie of dissolution of an additional gold rhombic dodecahedron exhibiting the tetrahexahedron transient intermediate and final cube shapes. The acquisition frame rate is 2.5 fps. The electron dose rate was 86 electrons/Å^2·s.

Movie S34. Monte Carlo simulation movie of a rhombic dodecahedral, 7-million-atom nanocrystal etched at the chemical potential $\frac{\mu}{\epsilon}$ = -6.5. The number of attempted Monte Carlo steps was ~1.24×10^8, and the acceptance ratio was ~5.04×10^{-2}. The nanocrystal is viewed along the ⟨110⟩ zone axis.

Movie S35. Monte Carlo simulation movie of a rhombic dodecahedral, 7-million-atom nanocrystal etched at the chemical potential $\frac{\mu}{\epsilon}$ = -6.5. The number of attempted Monte Carlo steps was ~1.24×10^8, and the acceptance ratio was ~5.04×10^{-2}. The nanocrystal is viewed along the ⟨110⟩ zone axis and the atoms are color-coded according to their coordination numbers.

Movie S36. Monte Carlo simulation movies of a rhombic dodecahedral, 7-million-atom nanocrystal etched at different values of the chemical potential: from left-to-right, top-to-bottom $\frac{\mu}{\epsilon}$ = -5.0, -5.98, -6.0, -6.25, -6.5, -6.75, -7.0, -8.0. The numbers of attempted Monte Carlo steps were: ~2×10^8, 2×10^{10}, 2.23×10^9, 1.34×10^8, 1.24×10^8, 1.17×10^8, 6.45×10^7, 3.60×10^7, respectively, and the corresponding acceptance ratios were: ~3.69×10^{-2}, 1.21×10^{-2}, 3.43×10^{-2}, 5.00×10^{-2}, 5.04×10^{-2}, 5.60×10^{-2}, 0.113, 0.179. The nanocrystals are viewed along the ⟨100⟩ zone axis.

Movie S37. Monte Carlo simulation movies of a rhombic dodecahedral, 7-million-atom nanocrystal etched at different values of the chemical potential: from left-to-right, top-to-bottom $\frac{\mu}{\epsilon}$ = -5.0, -5.98, -6.0, -6.25, -6.5, -6.75, -7.0, -8.0. The numbers of attempted Monte Carlo steps were: ~2×10^8, 2×10^{10}, 2.23×10^9, 1.34×10^8, 1.24×10^8, 1.17×10^8, 6.45×10^7, 3.60×10^7, respectively, and the corresponding acceptance ratios were: ~3.69×10^{-2}, 1.21×10^{-2}, 3.43×10^{-2}, 5.00×10^{-2}, 5.04×10^{-2}, 5.60×10^{-2}, 0.113, 0.179. The nanocrystals are viewed along the ⟨110⟩ zone axis.

Movie S38. Monte Carlo simulation movies of a rhombic dodecahedral, 7-million-atom nanocrystal etched at different values of the chemical potential: from left-to-right, top-to-bottom $\frac{\mu}{\epsilon}$ = -5.0, -5.98, -6.0, -6.25, -6.5, -6.75, -7.0, -8.0. The numbers of attempted Monte Carlo steps were: ~2×10^8, 2×10^{10}, 2.23×10^9, 1.34×10^8, 1.24×10^8, 1.17×10^8, 6.45×10^7, 3.60×10^7, respectively, and the corresponding acceptance ratios were: ~3.69×10^{-2}, 1.21×10^{-2}, 3.43×10^{-2}, 5.00×10^{-2}, 5.04×10^{-2}, 5.60×10^{-2}, 0.113, 0.179. The nanocrystals are viewed along the ⟨100⟩ zone axis and the atoms are color-coded according to their coordination numbers.

Movie S39. Monte Carlo simulation movies of a rhombic dodecahedral, 7-million-atom nanocrystal etched at different values of the chemical potential: from left-to-right, top-to-bottom $\frac{\mu}{\epsilon}$ = -5.0, -5.98, -6.0, -6.25, -6.5, -6.75, -7.0, -8.0. The numbers of attempted Monte Carlo steps were: ~2×10^8, 2×10^{10}, 2.23×10^9, 1.34×10^8, 1.24×10^8, 1.17×10^8, 6.45×10^7, 3.60×10^7, respectively, and the corresponding acceptance ratios were: ~3.69×10^{-2}, 1.21×10^{-2}, 3.43×10^{-2}, 5.00×10^{-2}, 5.04×10^{-2}, 5.60×10^{-2}, 0.113, 0.179. The nanocrystals are viewed along the ⟨110⟩ zone axis and the atoms are color-coded according to their coordination numbers.

Movie S40. TEM movie of simultaneous dissolution of a gold rhombic dodecahedron and cube exhibiting the tetrahexahedron transient intermediate shape. The acquisition frame rate is 2.5 fps. The electron dose rate was 86 electrons/$Å^2$·s.

Movie S41. TEM movie of partial dissolution of a gold triangular prism followed by surface re-faceting and homogeneous nucleation of small gold nanocrystals. The concentration of $FeCl_3$ was 0.02 M in the GLC loading solution, which was prepared by mixing 0.3 mL of 0.1 M acidified $FeCl_3$ and 1.2 mL of 0.01 M Tris buffer solution. The acquisition frame rate is 2.5 fps. The electron dose rate was 217 electrons/$Å^2$·s.

Movie S42. Contour plot movie showing the progression of nanocrystal local curvature for the equilibrium triangular prism dissolution reaction shown in Movie S41. Five contours are shown at any given time to better illustrate the development of low-energy blunt facets.

Movie S43. TEM movie of dissolution of a gold triangular prism exhibiting a complex transient intermediate morphology. The acquisition frame rate is 2.5 fps. The electron dose rate was 86 electrons/Å^2·s.

Movie S44. TEM movie of dissolution of an additional gold triangular prism exhibiting a complex transient intermediate morphology. The acquisition frame rate is 5.0 fps. The electron dose rate was 86 electrons/Å^2·s.

Movie S45. Monte Carlo simulation movies of a cubic, 1-, 7- and 55-million-atom nanocrystal etched at the chemical potential $\frac{\mu}{\epsilon}$ = -6.5. The numbers of attempted Monte Carlo steps were: ~1.94×10^7, 1.34×10^8, 1.10×10^9, respectively, and the corresponding acceptance ratios were: ~5.56×10^{-2}, 5.24×10^{-2}, 5.06×10^{-2}. The nanocrystals are viewed along the ⟨100⟩ zone axis. For the three movies at the bottom, the atoms are color-coded according to their coordination numbers.

Movie S46. Monte Carlo simulation movies of a rhombic dodecahedral, 1-, 7- and 55-million-atom nanocrystal etched at the chemical potential $\frac{\mu}{\epsilon}$ = -6.5. The numbers of attempted Monte Carlo steps were: ~2.03×10^7, 1.24×10^8, 1.05×10^9, respectively, and the corresponding acceptance ratios were: ~5.33×10^{-2}, 5.04×10^{-2}, 4.77×10^{-2}. The nanocrystals are viewed along the ⟨100⟩ zone axis. For the three movies at the bottom, the atoms are color-coded according to their coordination numbers.

Movie S47. Monte Carlo simulation movies of a rhombic dodecahedral, 1-, 7- and 55-million-atom nanocrystal etched at the chemical potential $\frac{\mu}{\epsilon}$ = -6.5. The numbers of attempted Monte Carlo steps were: ~2.03×10^7, 1.24×10^{-2} 1.05×10^9, respectively, and the corresponding acceptance ratios were: ~5.33×10^{-2}, 5.04×10^{-2}, 4.77×10^{-2}. The nanocrystals are viewed along the ⟨110⟩ zone axis. For the three movies at the bottom, the atoms are color-coded according to their coordination numbers.

Movie S48. TEM movie of rapid dissolution of a gold cube. The acquisition frame rate is 2.5 fps. The electron dose rate was 217 electrons/Å^2·s.

Movie ID	Content Description	Concentration of $FeCl_3$ (mol/L)	Electron dose rate (electrons/$Å^2$•s)	Acquisition frame rate (s/frame)
S1	Figure 1: Equilibrium nanorod etching	0.02	217	0.4
S2	Figure 1: Non-equilibrium nanorod etching	0.03	217	0.2
S3	Control experiment: No HCl, no $FeCl_3$	NA	217	0.4
S4	Control experiment: With HCl, no $FeCl_3$	NA	217	0.4
S5	Control experiment: Au@SiO_2 core-shell nanorod	0.04	217	0.4
S6	Control experiment: With isopropanol, lower dose rate	0.04	86	0.4
S7	Control experiment: With isopropanol, higher dose rate	0.04	254	0.4
S8	Control experiment: Lower $FeCl_3$ concentration	0.02	217	0.4
S9	Additional equilibrium nanorod etching	0.02	1500	0.025
S10	Figure 2: Nanorod	0.04	217	0.4
S12	Progression of contours for equilibrium nanorod etching shown in Movie S1	0.02	217	0.4
S13	Figure 2: Blunted rod	0.04	217	0.4
S14	Additional blunted rod	0.03	217	0.4
S15	Pentagonal bipyramid	0.04	217	0.2
S16	Tip-selective blunting: Decahedron	0.03	86	0.4
S17	Tip-selective blunting: Rhombic dodecahedron	0.03	86	0.4
S18	Tip-selective blunting: Triangular bipyramid	0.04	86	0.2
S19	Tip-selective blunting: Octahedron	0.03	86	0.4
S20	Triangular prism	0.04	217	0.4
S21	Pair of regular and blunted nanorod	0.04	217	0.4
S22	Figure 3: Cube	0.04	86	0.4
S23	Additional cube	0.04	86	0.4
S26	Equilibrium etching of cube to truncated octahedron	0.02	86	0.4
S27	Progression of contours for equilibrium cube etching shown in Movie S26	0.02	86	0.4
S32	Figure 3: Rhombic dodecahedron	0.04	86	0.4
S33	Additional rhombic dodecahedron	0.04	86	0.4
S40	Pair of rhombic dodecahedron and cube	0.04	86	0.4
S41	Equilibrium etching and re-faceting of a triangular prism	0.02	217	0.4
S42	Progression of contours for equilibrium triangular prism etching shown in Movie S41	0.02	217	0.4
S43	Triangular prism with faceted intermediate	0.04	86	0.4
S44	Additional triangular prism with faceted intermediate	0.04	86	0.2
S48	Cube etched with higher dose rate	0.04	217	0.4

Table S1. Summary of TEM movies and their acquisition parameters.

Movie ID	Content Description	System Size (# atoms)	Chemical Potential (μ/ε)
S11	Rod etching viewed along the ⟨100⟩ zone axis	2 million	-5.98, -6.5
S24	Cube etching viewed along the ⟨100⟩ zone axis	7 million	-6.5
S25	Cube etching (color-coded with *n*) viewed along the ⟨100⟩ zone axis	7 million	-6.5
S28	Cube: Effects of surface diffusion viewed along the ⟨100⟩ zone axis	1.3 million	NA
S29	Cube etching viewed along the ⟨100⟩ zone axis	7 million	-5.0 to -8.0
S30	Cube etching (color-coded with *n*) viewed along the ⟨100⟩ zone axis	7 million	-5.0 to -8.0
S31	Cube: idealized etching	NA	NA
S34	Rhombic dodecahedron etching viewed along ⟨110⟩ zone axis	7 million	-6.5
S35	Rhombic dodecahedron etching (color-coded with *n*) viewed along ⟨110⟩ zone axis	7 million	-6.5
S36	Rhombic dodecahedron etching viewed along ⟨100⟩ zone axis	7 million	-5.0 to -8.0
S37	Rhombic dodecahedron etching viewed along ⟨110⟩ zone axis	7 million	-5.0 to -8.0
S38	Rhombic dodecahedron etching (color-coded with *n*) viewed along ⟨100⟩ zone axis	7 million	-5.0 to -8.0
S39	Rhombic dodecahedron etching (color-coded with *n*) viewed along ⟨110⟩ zone axis	7 million	-5.0 to -8.0
S45	Cube etching viewed along the ⟨100⟩ zone axis	1, 7 and 55 million	-6.5
S46	Rhombic dodecahedron etching viewed along ⟨100⟩ zone axis	1, 7 and 55 million	-6.5
S47	Rhombic dodecahedron etching viewed along ⟨110⟩ zone axis	1, 7 and 55 million	-6.5

Table S2. Summary of Monte Carlo Simulation Movies and their parameters.

S5. Supplementary References

1. G. S. Rohrer, *Structure and Bonding in Crystalline Materials*. (Cambridge University Press, Cambridge, UK, 2001).
2. X. Ye, C. Zheng, J. Chen, Y. Gao, C. B. Murray, *Nano Lett.* **13**, 765-771 (2013).
3. B. Nikoobakht, M. A. El-Sayed, *Chem. Mater.* **15**, 1957-1962 (2003).
4. Liu, P. Guyot-Sionnest, *J. Phys. Chem. B* **109**, 22192-22200 (2005).
5. M. R. Jones, C. A. Mirkin, *Angew. Chem., Int. Ed.* **52**, 2886-2891 (2013).
6. M. N. O'Brien, M. R. Jones, K. A. Brown, C. A. Mirkin, *J. Am. Chem. Soc.* **136**, 7603-7606 (2014).
7. G. V. Buxton, C. L. Greenstock, W. P. Helman, A. B. Ross, *J. Phys. Chem. Ref. Data* **17**, 513-886 (1988).
8. E. Sutter, K. Jungjohann, S. Bliznakov, A. Courty, E. Maisonhaute, S. Tenney, P. Sutter, *Nat. Commun.* **5**, (2014).
9. Q. Chen, J. M. Smith, J. Park, K. Kim, D. Ho, H. I. Rasool, A. Zettl, A. P. Alivisatos, *Nano Lett.* **13**, 4556-4561 (2013).
10. D. Chandler, *Introduction to Modern Statistical Mechanics*. (Oxford University Press, New York, 1987).
11. R. J. Glauber, *J. Math. Phys.* **4**, 294-307 (1963).
12. W. P. Davey, *Phys. Rev.* **25**, 753-761 (1925).
13. D. W. Oxtoby, *J. Phys.: Condens. Matter* **4**, 7627 (1992).
14. S. Schneider, A. Surrey, D. Pohl, L. Schultz, B. Rellinghaus, *Micron* **63**, 52-56 (2014).
15. Z. Nie, D. Fava, E. Kumacheva, S. Zou, G. C. Walker, M. Rubinstein, *Nat. Mater.* **6**, 609-614 (2007).
16. P. Zijlstra, P. M. R. Paulo, K. Yu, Q.-H. Xu, M. Orrit, *Angew. Chem., Int. Ed.* **51**, 8352-8355 (2012).
17. G. Z. Wulff, *Kristallog.* **34**, 449 (1901).
18. J. Krug, in *Multiscale Modeling in Epitaxial Growth,* A. Voigt, Ed. (Birkhäuser Basel, Basel, 2005), pp. 69-95.
19. W. K. Burton, N. Cabrera, F. C. Frank, *Philos. Trans. R. Soc. London, A* **243**, 299-358 (1951).
20. N. Tian, Z.-Y. Zhou, S.-G. Sun, Y. Ding, Z. L. Wang, *Science* **316**, 732-735 (2007).
21. Z. Y. Zhou, N. Tian, Z. Z. Huang, D. J. Chen, S. G. Sun, *Faraday Discuss.* **140**, 81-92 (2008).
22. J. Xiao, S. Liu, N. Tian, Z.-Y. Zhou, H.-X. Liu, B.-B. Xu, S.-G. Sun, *J. Am. Chem. Soc.* **135**, 18754-18757 (2013).
23. B. Lim, M. Jiang, J. Tao, P. H. C. Camargo, Y. Zhu, Y. Xia, *Adv. Funct. Mater.* **19**, 189-200 (2009).
24. T. K. Sau, C. J. Murphy, *J. Am. Chem. Soc.* **126**, 8648-8649 (2004).
25. C. J. Johnson, E. Dujardin, S. A. Davis, C. J. Murphy, S. Mann, *J. Mater. Chem.* **12**, 1765-1770 (2002).
26. D. P. Landau, K. Binder, *A Guide to Monte Carlo Simulations in Statistical Physics*. (Cambridge University Press, Cambridge, UK, 2000).